THESIS FOR THE DEGREE OF DOCTOR OF PHILOSOPHY

GPS Meteorology: With Focus on Climate Applications

TONG NING

CHALMERS

Department of Earth and Space Sciences
Chalmers University of Technology
Gothenburg, Sweden 2012

GPS Meteorology: With Focus on Climate Applications
TONG NING
ISBN 978-91-7385-675-1

Doktorsavhandlingar vid
Chalmers Tekniska Högskola
Ny serie Nr 3356
ISSN 0346-718X

Department of Earth and Space Sciences
Chalmers University of Technology
SE-412 96 Gothenburg, Sweden
Telephone +46 (0)31-772 1000

Cover:
Linear trends in the atmospheric water vapour content estimated from 42 globally distributed GPS sites for the time period from 1 January 1997 to 31 December 2011. The red circles mean positive trends and the blue circles mean negative trends. The size of the circle depends on the value of the trend. See details in Section 4.1.

Printed by Chalmers Reproservice
Chalmers University of Technology
Gothenburg, Sweden 2012

To the person I love

GPS Meteorology: With Focus on Climate Applications

TONG NING
Department of Earth and Space Sciences
Chalmers University of Technology

Abstract

The vital role of water vapour in the Earth's climate system requires measurements of the atmospheric Integrated Water Vapour (IWV) with a long-term stability and a high accuracy. This work focuses on using the Global Positioning System (GPS) to provide IWV estimates for climate applications. The advantages of the GPS measurements are that they can be performed independently on the weather and have a high temporal resolution (a few minutes) as well as a continuously improving spatial resolution (a few km for some local networks). The uncertainty of the GPS-derived IWV highly depends on the accuracy of the estimated Zenith Total Delay (ZTD), which is determined by many parameters, i.e. satellite orbit errors, ionospheric delay, signal multipath, antenna related errors (e.g. phase centre variations), and mapping functions. We demonstrated that the uncertainty of the GPS-derived IWV below 1 kg/m^2 is achievable.

The long-term change of the IWV can be an independent data source to detect climate changes. Using a global GPS IWV data set covering a 15-year-long time period, we found estimated IWV trends in a range from -1.65 to $+2.32$ kg/(m^2·decade) which, however, are comparable to the trend uncertainties varying from 0.21 to 1.52 kg/(m^2·decade). The trend uncertainty is mainly caused by the short-term variations of the IWV which cannot be modelled accurately. The uncertainty is also due to the errors in IWV estimates, which are random and/or elevation-dependent systematic errors. A higher elevation cutoff angle used in the GPS data analysis (a 25° was revealed for the time period investigated and for the region of Fennoscandia) can be an advantage to reduce the impact of such systematic errors.

The GPS-derived IWV can also be used for the evaluation of climate models. The IWV derived from the GPS measurements acquired at 99 European sites, each with a maximum time series of 14 years, were compared to the IWV simulated by a regional climate model. Overall, a monthly mean difference of $\sim$0.5 kg/m^2 (model$-$GPS) is obtained where a significant seasonal variation is seen in the difference. The model is too dry in the summer. Study of the diurnal cycle of the IWV using both the GPS data and the model simulation shows a good agreement for the phase while a smaller amplitude is seen in the results from the model.

Keywords: atmospheric Integrated Water Vapour, Global Positioning System, regional climate model, Zenith Total Delay.

Acknowledgements

Time flies. I have been studying at Chalmers for almost five years which for me is just like the blink of an eye. Now it is time to summarize my study. Before that, I would like to first express my thanks to all people who are behind me during those years. Without you, this thesis would not exist.

My most sincere thanks and warm gratitude go to my supervisor Gunnar Elgered for his continuous support, unlimited patience and nice personality, as well as the comfortable environment you made when we have a discussion. You really know how to encourage your students moving forward.

Thanks to Jan Johansson for bringing me to the GIPSY world. In my opinion, GIPSY is the best GPS processing software. :)

I like to express my special thanks to Lubomir Gradinarsky for introducing me to the Geo-group.

Big thanks to all present and former members of the Geo-group: Rüdiger Haas, Hans-Georg Scherneck, Johan Löfgren, Per O. J. Jarlemark, T. Ragne Emardson, Tobias Nilsson, and Martin Lidberg.

All staff and students at the observatory are thanked for the pleasant working atmosphere. Special thanks to Roger Hammargren for always helping me fix the computer problems.

Thanks to Junhong Wang and Liangying Zhang for their hospitality and for giving me access to their work and data during the two month visit to NCAR.

My deep gratitude goes to the friends back to my hometown: Qi Ning, He Zhenzhen, Huang Yanlan, Liang Tong, Liu Huahui, Luo Jiepin, Wu Guoyi, Wu Xin, Zeng Ling. Without your encourage and unselfish support, I would not start my study abroad.

Many many thanks to all my friends, new and old, in Sweden: Haoran, Wei, Xiaoming, Xuezhi, Yiqi, Yiyu, You, Zhennan, and ..., for being around me. It would be too long to list all of your names here, but I am sure that you know who you are!

The financial support for my position was supported by VINNOVA, the Swedish Governmental Agency for Innovation Systems, through the project P29459-1 “Long Term Water 216 Vapour Measurements Using GPS for Improvement of Climate Modelling”.

LIST OF PUBLICATIONS

Appended papers

Paper A
Ning, T., R. Haas, G. Elgered, and U. Willén, Multi-technique comparisons of ten years of wet delay estimates on the west coast of Sweden, *Journal of Geodesy*, in press, doi:10.1007/s00190-011-0527-2, 2012.

Paper B
Ning, T., G. Elgered, and J.M. Johansson, The impact of microwave absorber and radome geometries on GNSS measurements of station coordinates and atmospheric water vapour, *Advances in Space Research*, vol. 47, no. 2, pp. 186–196, doi:10.1016/j.asr.2010.06.023, 2011.

Paper C
Ning, T. and G. Elgered, Trends in the atmospheric water vapor content from ground-based GPS: the impact of the elevation cutoff angle, *IEEE Journal of Selected Topics in Applied Earth Observations and Remote Sensing*, vol. 5, no. 3, in press, doi:10.1109/JSTARS.2012.2191392, 2012.

Paper D
Ning, T., G. Elgered, U. Willén, and J.M. Johansson, Evaluation of the atmospheric water vapor content in a regional climate models using ground-based GPS measurements, *Journal of Geophysical Research*, submitted May 6, 2012.

LIST OF PUBLICATIONS

Other related papers

Ning, T., J.M. Johansson, H.-G. Scherneck, P.O.J. Jarlemark, and R. Emardson, High-rate GNSS techniques for the detection of large seismic displacements, *Proceedings of the 2009 IEEE International Geoscience and Remote Sensing Symposium*, 359–362, 13–17 July, Cape Town, South Africa, 2009.

Ning, T., G. Elgered, and J.M. Johansson, The impact of microwave absorber and radome geometries on geodetic measurements with ground-based GNSS antennas, *Proc. of 2nd Colloquium Scientific and Fundamental Aspects of the Galileo Programme*, European Space Agency, 15–19 October, Padua, Italy, 2009.

Haas, R., T. Ning, and G. Elgered, Observation of long term trends in the amount of atmospheric water vapor by space geodesy and remote sensing techniques, *Proceedings of the 2010 IEEE International Geoscience and Remote Sensing Symposium*, 2,944–2,947, ISBN/ISSN:978-1-4244-9564-1, 2010.

Elgered, G., T. Ning, J.M. Johansson, U. Willén, E. Kjellström, P.O.J. Jarlemark, R. Emardson, and T. Nilsson, Evaluation of climate models using ground-based GNSS observations, *Proceedings of the General Assembly of the Nordic Geodetic Commission*, 26–30 September, Norway, 2010.

Ning, T. and G. Elgered, Monitoring long term variability in the atmospheric water vapour content using ground-based GPS receiver networks, *Proceedings of the 3rd International Colloquium-Scientific and Fundamental Aspects of the Galileo Programme*, 31 August–2 September, Copenhagen, Denmark, 2011.

Haas, R., T. Ning, and G. Elgered, Long-term trends in the amount of atmospheric water vapour derived from space geodetic and remote sensing techniques, *Proceedings of the 3rd International Colloquium-Scientific and Fundamental Aspects of the Galileo Programme*, 31 August–2 September, Copenhagen, Denmark, 2011.

Contents

Chapter 1

Introduction

1.1 The role of water vapour in the climate system

Water vapour is water in the gaseous phase. It is one state of water within the hydrosphere. Through the hydrological cycle, water vapour constantly enters the atmosphere by evaporation, forms clouds by condensation, and subsequently comes back to the Earth's surface by precipitation (*Bengtsson et al.*, 2010). The whole cycle is an important mechanism for transferring heat energy from the Earth's surface to its atmosphere and in moving heat around the Earth. In addition to its role in the water budget, water vapour is also a very important greenhouse gas due to its ability of absorbing long wave thermal radiation emitted from the Earth's surface. A warmer climate increases the amount of water vapour, which further reduce the amount of long-wave radiation escaping from the Earth to space, and thereby leading to an even warmer climate. Hence, the atmospheric water vapour is very important for the Earth's climate system and a key to understand the hydrological cycle.

1.1.1 Hydrological cycle

Vapour, liquid, and solid are the three states of water in our planet. The transfer of water in all three states are described by the hydrological cycle occurring within and between the Earth's atmosphere, oceans, and continents (*Trenberth et al.*, 2007). In the vapour state and associated with the evaporation and condensation, water moves quickly through the atmosphere and redistributes energy. The movement of water vapour through the hydrological cycle is strongly coupled to precipitation and soil moisture, which have important practical implications. Therefore, if we have sufficiently good observations of water vapour, we can understand details of the hydrological cycle.

The key role of the water vapour in the Earth's energy balance is stressed by *Bengtsson et al.* (2010). They pointed out that almost 50 % of the absorbed solar radiation at the surface is used to cool the surface, through evaporation, and warm the atmosphere, through the release of latent heat. In addition, *Bevis et al.* (1992) highlighted the importance of the distribution of the water vapour for the vertical stability of the atmosphere and the structure and evolution of storm systems. *Kou et al.* (1993) also indicated that assimilating water vapour observations into numerical weather models would significantly improve short-term forecasts of precipitation.

1.1.2 Greenhouse effect

The greenhouse effect is of great importance for the Earth's climate without which our Earth would be much colder than what we have now (*Greenhouse Gases and Greenhouse Effect*, 2003). When the visible light from the Sun (short wave radiation) reaches the surface of the Earth, it is absorbed and is converted to heat (long wave infrared thermal radiation), which eventually is radiated back into the atmosphere towards space. Greenhouse gases, i.e. water vapour, carbon dioxide, methane, etc., allow the Sun's short wave radiation to pass through them, but absorb the long wave infrared thermal radiation from the surface of the Earth. The greenhouse effect slows down the loss of heat and keeps the Earth's surface warmer. If we do not have the greenhouse gases, the Earth's atmosphere would be an average of about 30–35 °C cooler.

Compared to other greenhouse gases, water vapour is the most important one and accounts for 75 % of the total greenhouse effect on the Earth (*Kondratev*, 1972). Figure 1.1 depicts that the percentage absorption of the radiations, both from the Sun and the surface of the Earth, by water vapour and carbon dioxide. It is evident that water vapour dominates the absorption. According to *Buehler et al.* (2006), an increase of 20 % of the water vapour in the tropics would result in approximately the same impact as a doubling of the carbon dioxide concentration. It should be noted that water vapour is the major source of the natural greenhouse effect. The direct human influence on water vapour is almost negligible (*Intergovernmental Panel on Climate Change*, 2007), and the amount of water vapour moved to the atmosphere is rather from natural sources. However, this natural effect will be amplified due to that the emission of other greenhouse gases will increase temperature, which in turn results in an increase of water vapour since the equilibrium vapour pressure increases with increasing temperature.

1.1.3 Long-term trends

As water vapour is regulated by the temperature, global warming will have an impact on it. Assuming conservation of relative humidity, the changes in the atmospheric

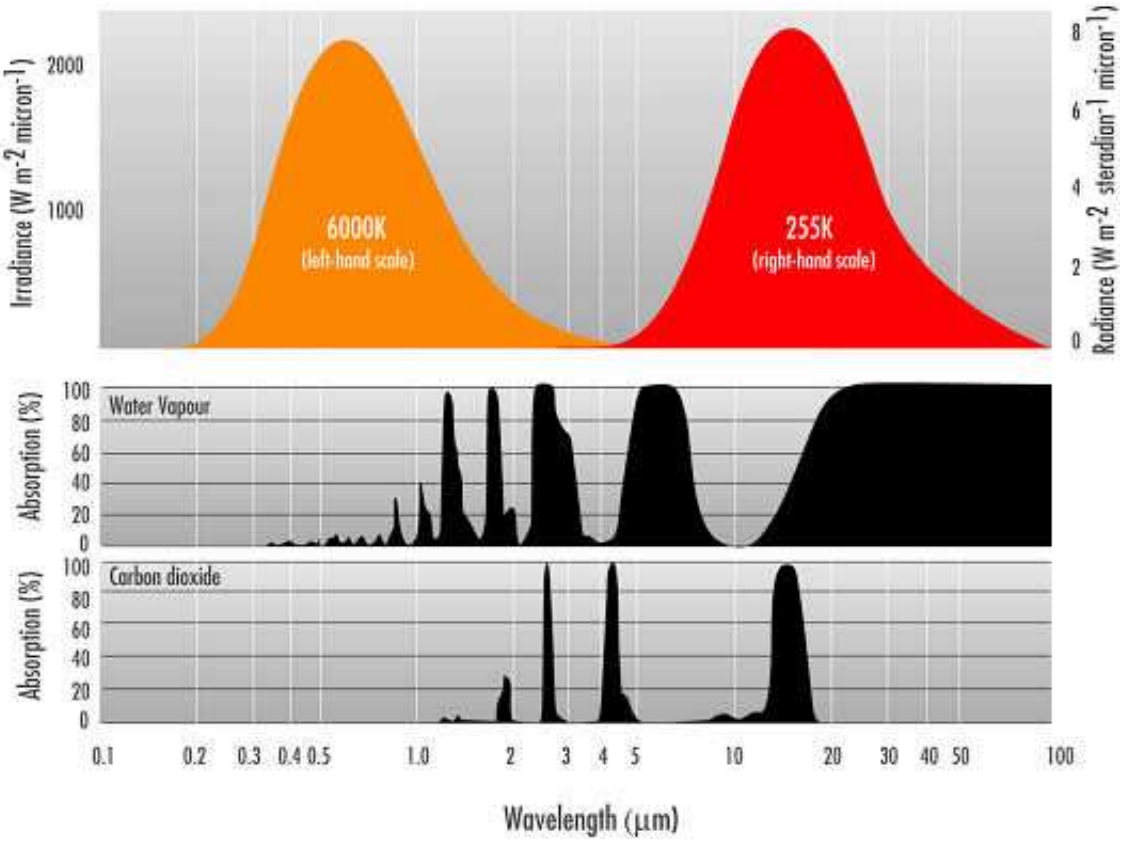

Figure 1.1: The radiation absorption characteristics of water vapour and carbon dioxide as a function of wavelength (source: `http://www.bom.gov.au/info/climate/change/gallery/4.shtml`). The upper portion of the chart depicts the wavelength distribution of radiation emitted from black bodies radiating at 6,000 K (approximately the solar photosphere) and 255 K (approximately the Earth's planetary temperature), with the solar irradiance measured at the mean distance of the Earth from the Sun. The percentage absorption of a vertical beam by representative atmospheric concentrations of water vapour and carbon dioxide are shown in the lower panels.

water vapour are related to a change in the temperature with a ratio of approximately 7 %/K (*Trenberth et al.*, 2003). This relationship was also investigated by *Mears et al.* (2007) where an increase of the temperature of 1 K results in an increase of water vapour by 5–7 %. Therefore, the long-term trend in the atmospheric water vapour can be used as an independent data source to assess possible global warming scenarios.

Traditionally, the long-term observations of the atmospheric water vapour are provided by radiosondes. *Ross and Elliot* (1996, 2001) found positive trends in the

water vapour over China, the Pacific Islands, and North America except for the northeastern part of Canada as well as a mixture of positive and negative trends over the most part of Eurasia, using the radiosonde data for the time period from 1973 to 1995. *Gaffen et al.* (1992) estimated the trends of the water vapour for 50 globally distributed radiosonde sites during the time period from 1973 to 1990. The results illustrated positive trends for most of the sites. The major disadvantage of using radiosondes for trend estimation is the systematic errors caused by either calibration uncertainties or sensor changes (*Wang and Zhang*, 2008).

A relative new method, using ground-based observations from the Global Position System (GPS), can provide long-term water vapour estimates with a high accuracy. Earlier studies made by *Gradinarsky et al.* (2002) and *Elgered et al.* (2003) found an increase of the atmospheric water vapour of 7–14 % per decade over Scandinavia for the time period 1993–2002. Another study for the same area, but for the time period from 1996 to 2006 was carried out by *Nilsson and Elgered* (2008). They also found positive trends in general.

1.2 Measurements of the atmospheric water vapour

Two parameters are normally used to refer to the atmospheric water vapour content. Definitions are reviewed by *Bevis et al.* (1992). One is the Integrated Water Vapour (IWV), denoted by V, defined as:

$$V = \int_0^\infty \rho_v(h)\, dh = \frac{1}{R_w} \int_0^\infty \frac{p_w(h)}{T(h)}\, dh \tag{1.1}$$

where ρ_v is the absolute humidity in kg/m^3; the height h is expressed in metres; R_w is called the specific gas constant for water vapour and equals to 461.522 $\pm$ 0.008 J/(kg·K) (`http://physics.nist.gov/cuu/Constants/index.html`); p_w is the partial pressure of water vapour in hPa and T is the absolute temperature in K. Normally, IWV refers to the quantity of the atmospheric water vapour over a specific location (e.g. the ground GPS site). The other parameter is the Precipitable Water (PW), denoted by W, which expresses the height of an equivalent column of liquid water in units of length. The two parameters are exchangeable using the relation:

$$W = \frac{V}{\rho_w} \tag{1.2}$$

where ρ_w is the density of liquid water and equals to 1000 $\pm$ 0.002 kg/m^3 (*Wolf*, 2008). The parameter IWV, in units of kg/m^2, is used throughout this thesis.

A variety of systems exist for measuring the atmospheric IWV, which can be divided into different categories, e.g. in situ measurements, ground-based up-looking measurements, and satellite-based down-looking measurements.

1.2.1 In situ measurements

A radiosonde is a balloon-borne instrument which can provide vertical profile information of the atmospheric IWV. The radiosonde has been one of the most important devices given its long observation history (*Ross and Elliot* (1996, 2001)). However, the accuracy of the radiosonde-derived IWV is lower at high altitude, and the role of the radiosonde data for climate research is limited due to instrument instabilities (details are given in Section 2.1).

1.2.2 Ground-based measurements

As shown in Figure 1.1, radiation of different wavelengths, from the Sun and the surface of the Earth is absorbed by the atmospheric water vapour and some is re-emitted back to the ground. The absorbed and re-emitted radiation can be estimated from the measurements carried out in different frequency bands, which are at and around the water vapour spectral lines. The estimated absorbed and re-emitted radiation then can be used to infer the amount of the atmospheric water vapour. Instruments working in such way include:

- A ground-based microwave radiometer (often referred to as a Water Vapour Radiometer (WVR)) is a upward-looking device which can infer the IWV along the direction of the observation based on the measured microwave radiation from the atmospheric water vapour. A WVR cannot work during rain. A detailed discussion about WVR observations is given in Section 2.2.3.

- A sun photometer can track the Sun and measure direct sunlight along the line of sight in different channels. Using the one which is centred on the water vapour absorption line, the water vapour transmittance can be determined after first accounting for aerosol effects. The transmittance is then converted to the IWV using a method based on radiative transfer modelling (*Ingold et al.*, 2000). A sun photometer works under cloud-free conditions.

More recently, based on the path delay when radio waves propagate through the neutral atmosphere of the Earth, the IWV can be inferred from the ground-based observations from GPS and Very Long Baseline Interferometry (VLBI). Both the VLBI and the GPS techniques are discussed in detail in Sections 2.2.4 and 2.2.5, respectively.

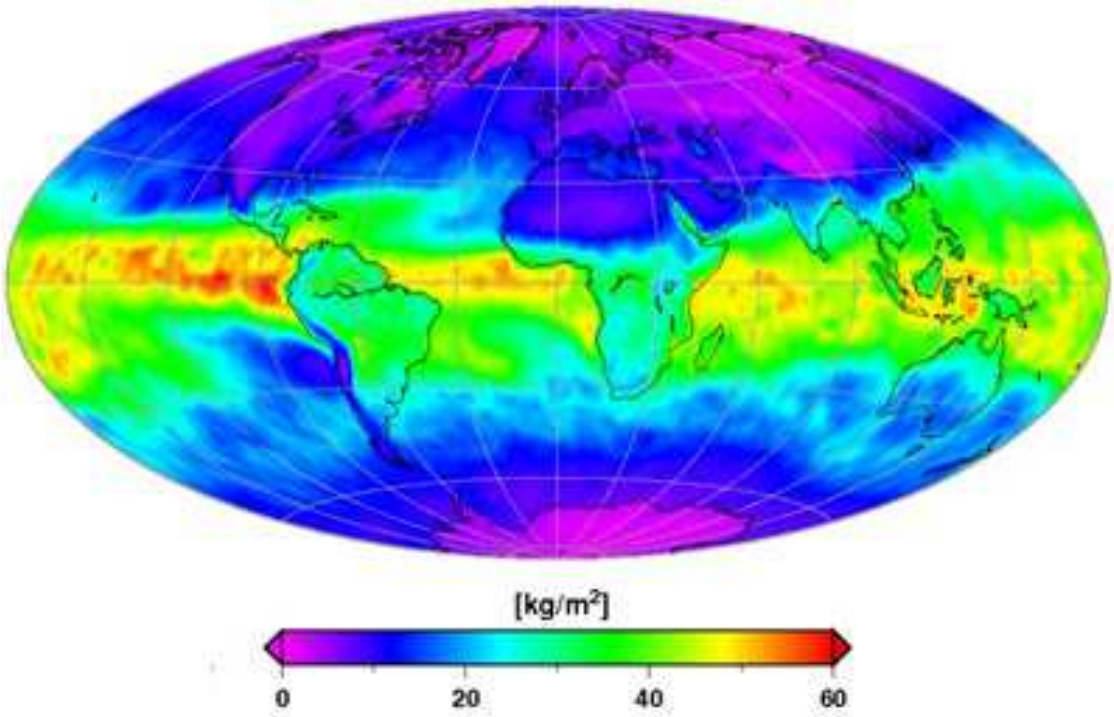

Figure 1.2: The global distribution of the IWV in March 2010 obtained from satellite observations (source: `http://www.eumetsat.int/Home/Main/News/Features/717482`).

1.2.3 Satellite-based measurements

Measurements of the atmospheric water vapour from space can be performed using down-looking sensors on a satellite, such as infrared sensors (*Chaboureau et al.*, 1998), microwave sensors (*Jury and Waliser*, 1990), and GPS receivers on Lower Earth Orbiting (LEO) satellites observing GPS satellites during occultation (*Heise et al.*, 2006).

The IWV obtained from satellite measurements can have a global coverage if the satellites fly over every "point" of the Earth within a specified time frame. However, a so called "point" for a satellite observation may mean an area of several hundreds of square kilometres. Therefore, only IWV averaged over a very large area can be provided by satellite measurements. Figure 1.2 depicts an example of the globally distributed IWV for March, 2010 obtained from the Microwave Humidity Sounder (MHS), a satellite-based radiometer operating in the frequency range from 89 GHz to 190 GHz. Depending on what sensors are used, satellite observations may not provide data under all weather conditions. On the other hand, satellite observations give high accuracy over oceanic regions, which otherwise are very difficult to cover efficiently for ground-based measurements.

1.3 Thesis structure

Chapter 2 introduces four IWV measurement techniques: radiosondes, WVR, GPS, and VLBI. The path delay of radio waves propagating through the neutral atmosphere is described, especially the wet delay which is caused by the atmospheric water vapour. Comparisons of ten years of wet delay estimates obtained from these four techniques, located on the west coast of Sweden, are presented in Paper A.

All GPS measurements are subject to error sources. The impact of the elevation-dependent errors, i.e. antenna phase centre variations and multipath effects, is investigated by Paper B. In order to interpret GPS measurements correctly and draw valid conclusions on the quality of the resulting IWV estimates, the uncertainty of the GPS-derived IWV are evaluated in Chapter 3, where two methods, referred to as a statistical and a theoretical analysis, are presented.

The use of the GPS technique for climate applications is discussed in Chapter 4. Given its long-term stability and the continuously increasing time series, GPS-derived IWV is likely to become a preferred technique to estimate any long-term trends in the atmospheric water vapour. The uncertainty of the resulting trend, caused by both the short-term IWV variation (the natural variability of the weather) and the uncertainty of the IWV estimate, is investigated in Paper C. Since currently the GPS data have not yet been assimilated in any climate reanalysis products, it is also appropriate as an independent data set for evaluation of climate models. Paper D presents the results of using GPS-derived IWV to evaluate the IWV simulated by the regional Rossby Centre Atmospheric (RCA) climate model which runs using the European Centre for Medium-range Weather Forecasts (ECMWF) reanalysis data as boundary conditions.

Finally, the conclusions are presented in Chapter 5.

Chapter 2

Measurement Techniques

2.1 Radiosonde

A radiosonde is a traditional measurement device for upper air observations in meteorology. A radiosonde is equipped with different sensors (Figure 2.1a), which typ-

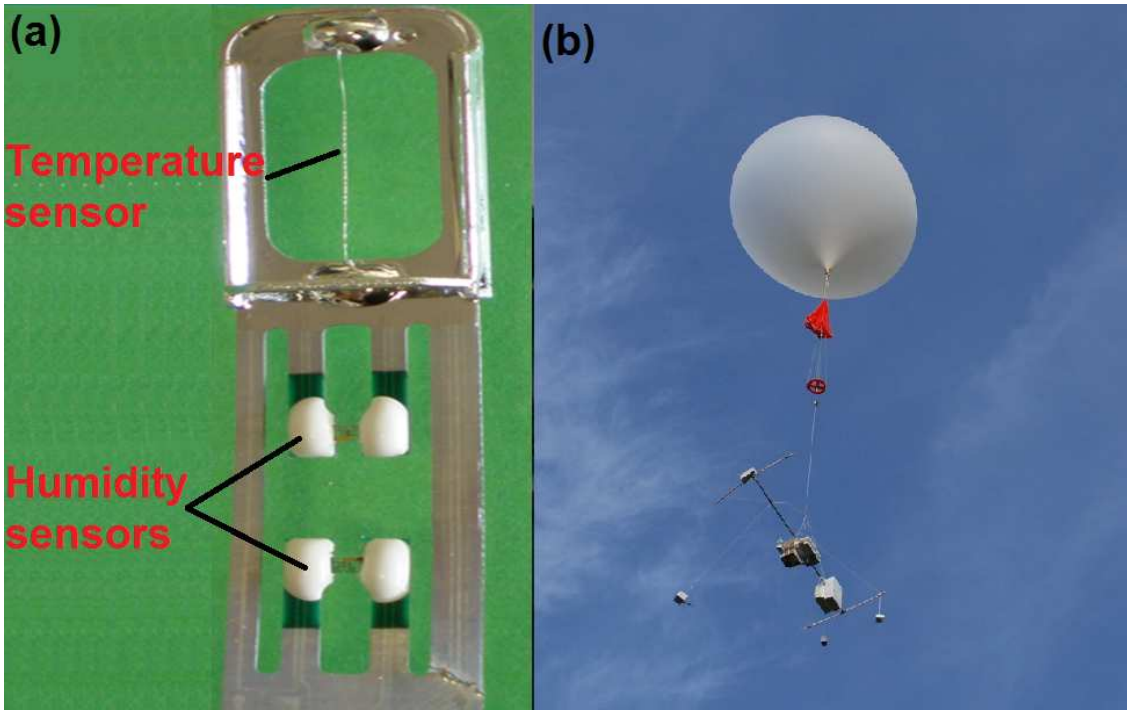

Figure 2.1: (a) Sensors of the Vaisala RS92 radiosonde with the temperature sensor in the upper and humidity sensors in the lower part and (b) a weather balloon with radiosondes (source: `http://www.dwd.de/bvbw/generator/DWDWWW/Content/Projekte/Gruan/Images/luami_2_en,templateId=poster,property=poster.jpg`).

ically measure pressure, temperature, relative humidity, and wind (both speed and direction). All radiosonde sensors together with a radio transmitter are attached to a weather balloon (Figure 2.1b), which is normally launched at the most four times per day (but more common is two times per day) and the measured vertical profiles of all parameters are reported back to a receiving site at the nominal time epochs 0:00, 6:00, 12:00, and 18:00 UTC. The integration of the vertical absolute humidity (expressed in units of kg/m^3) profiles from the surface to the top of the radiosonde profiles gives the atmospheric IWV.

Although radiosonde data provide a long and continuous water vapour time series (for the last six decades), the radiosonde-derived IWV suffers from errors partly due to the sensor characteristics that vary in time and space (*Wang and Zhang*, 2008). Meanwhile, due to sensor changes and lower requirement for long-term stability and traceability, radiosonde data are limited for climate research (*Titchner et al.*, 2009). For the last 15 years, globally the most commonly used sensor packages were the Vaisala RS80 and the Vaisala RS92. The specifications from the manufacturer state that the RS80 has a reproducibility of better than 3 % (one standard deviation in the relative humidity) and an additional 2 % uncertainty from the calibration. Assuming that they are independent errors results in a root-sum-squared value of 3.6 % for the total uncertainty. The corresponding numbers for the RS92 are 2 % and 1 %, resulting in a total uncertainty of 2.2 %. The assumption of normal distributed independent errors is likely optimistic. Therefore, a larger uncertainty may be more realistic. During measurements, systematic observational errors may be caused due to, e.g. time lag and solar radiation error (*Wang and Zhang*, 2008 and *Miloshevich et al.*, 2009). Based on the comparisons with globally distributed ground-based GPS measurements, *Wang and Zhang* (2008) found that both Vaisala instruments introduce a dry bias in its humidity measurements of around 5 % of the absolute value. An empirical correction was presented by *Miloshevich et al.* (2009) in order to remove the biases. They found that the uncertainty of the corrected bias from the RS92 measurements was approximately $\pm$ 4 % of the measured Relative Humidity (RH) value for nighttime and $\pm$ 5 % for daytime.

Figure 2.2 depicts the IWV estimates obtained from the radiosonde data acquired at Gothenburg-Landvetter Airport from January 1997 to December 2006. The IWV uncertainties are assumed to be 4 % of the absolute value and no systematic observational errors were considered.

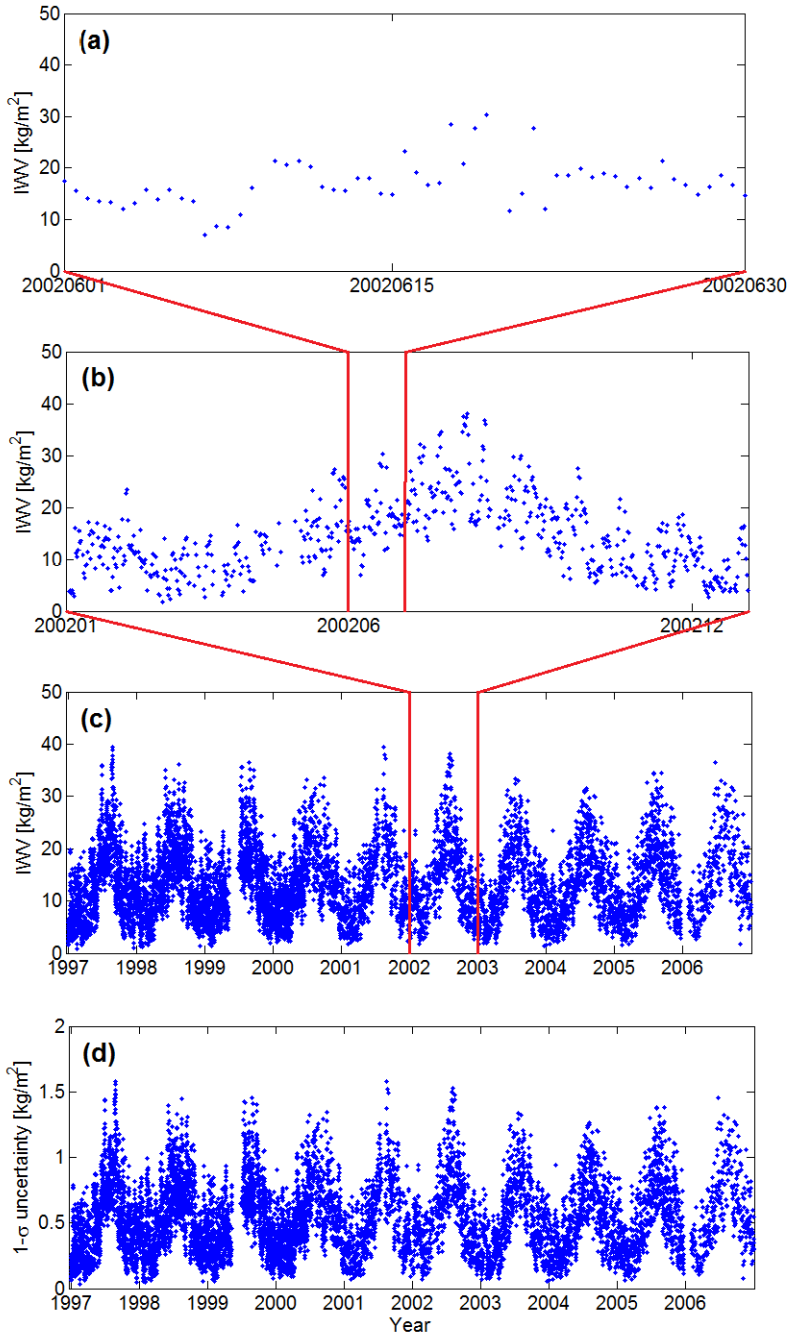

Figure 2.2: Time series of the IWV derived from the radiosondes launched at the Gothenburg-Landvetter Airport on the west coast of Sweden for (a) the month of June, 2002, (b) the year of 2002, (c) the time period from January 1997 to December 2006, and (d) the 1-σ uncertainty for the corresponding time period. Before February 2006, the radiosonde sensor used was the Vaisala RS80, which thereafter was replaced by the Vaisala RS92.

2.2 Radio techniques

In this section, three techniques, the Global Positioning System (GPS), Very Long Baseline Interferometry (VLBI), and the Water Vapour Radiometer (WVR) will be introduced. They are all capable of measuring the path delay of radio waves propagating through the neutral atmosphere. The wet delay, caused by the water vapour in the atmosphere, can be either measured based on the delay of radio waves (GPS and VLBI) or inferred from the atmospheric emission (WVR). The IWV in the atmosphere can be inferred from the estimated wet delay.

2.2.1 Radio wave delay through the neutral atmosphere

When a radio wave propagates through the neutral atmosphere, due to that the refractive index (n) is larger than 1, it will propagate along the path S instead of the geometrical path G (Figure 2.3). The resulting path length L is referred to as the electrical path and it is the electrically shortest distance due to the fact that signal otherwise would travel a longer distance along G with lower velocity close to the surface of the Earth where the index of refraction is larger (*Elgered*, 1993):

$$L = \int_S n(s)\, ds \tag{2.1}$$

The difference between L and G is normally defined as the path delay and can be

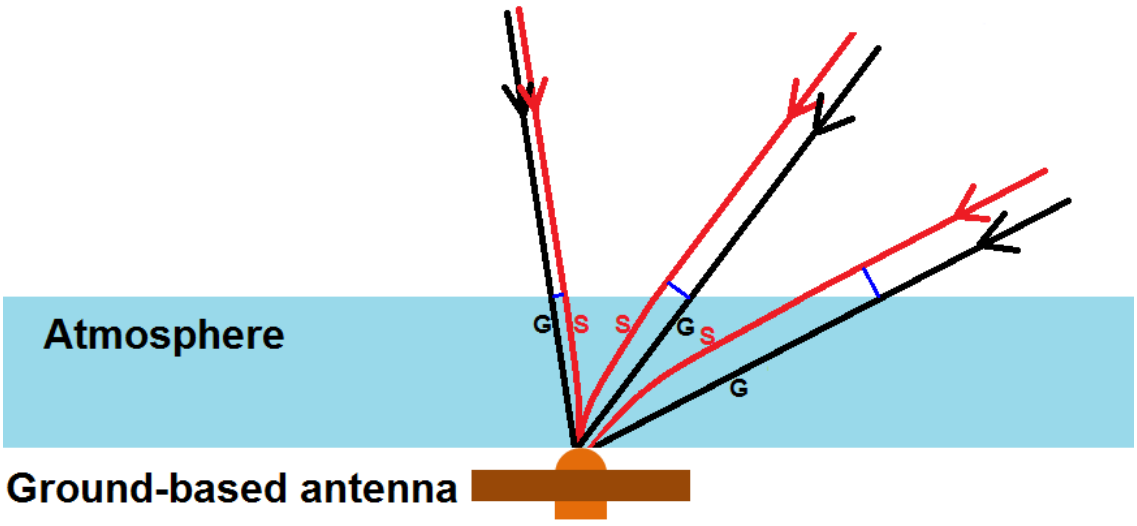

Figure 2.3: The signals from space will propagate to the ground-based antenna along the electrical paths (red lines), instead of the geometrical paths (black lines).

expressed as:

$$\triangle L(\epsilon, \phi) = \int_S n(s)\, ds - G \tag{2.2}$$

As shown in Figure 2.3, the path delay is getting larger as the elevation angle (ϵ) decreases where radio waves pass through more atmosphere. Due to an inhomogeneous atmosphere, for a given ϵ, the path delay can also be different for different azimuth angles (ϕ).

Equation (2.2) can be rewritten as:

$$\triangle L(\epsilon, \phi) = \int_S (n(s) - 1)\, ds + S - G \tag{2.3}$$

where the term S–G is often referred as the geometric delay due to bending. The geometric delay is zero in the zenith direction if the atmosphere is horizontally stratified and it can reach 10 cm at a lower elevation angle of 5°. The first term in Equation (2.3) is the path delay caused by the refractive index, which is the dominating term. For convenience, we can define the refractive index (n) using the refractivity (N):

$$N = 10^6\,(n - 1) \tag{2.4}$$

and ignore the second term (since it is zero in the zenith direction, it is normally included in the model, describing the elevation dependence, the so called mapping function) of Equation (2.3), which gives:

$$\triangle L(\epsilon, \phi) = 10^{-6} \int_S N(s)\, ds \tag{2.5}$$

The refractivity (N) is determined by the refractive index of the gases in the atmosphere, which can be divided into the wet (due to water vapour) and the dry (due to the rest of gases) part. An expression for N is given by *Owens* (1967):

$$N = k_1 \frac{p_d}{T} Z_d^{-1} + k_2 \frac{p_w}{T} Z_w^{-1} + k_3 \frac{p_w}{T^2} Z_w^{-1} \tag{2.6}$$

where p_d and p_w are the partial pressure of the dry gases and the water vapour in hPa, respectively; T is the physical temperature in K; Z_d^{-1} and Z_w^{-1} are the inverse compressibility factors for dry gases and water vapour, respectively. The values of k_1, k_2, and k_3 can be estimated from laboratory experiments. In Equation (2.6), the first term is the dry part of refractivity caused by the induced dipole moment of the dry gases while the wet part is given by the second and the third terms due to the induced dipole moment and the permanent dipole moment of the water vapour molecule, respectively. Since the hydrostatic equation is only valid for the total

Table 2.1: Values and uncertainties for k_1, k_2, k_3, and k_2'

Constant	Value[a]	Uncertainty[a]	Units
k_1	77.60	0.05	K/hPa
k_2	77.4	2.2	K/hPa
k_3	373900	1200	K^2/hPa
k_2'	22.1	2.2	K/hPa

[a]The values and uncertainties were taken from Table 1 in *Bevis et al.* (1994).

pressure, but not for the partial pressure of dry gases, a more useful expression for N therefore is given by *Davis et al.* (1985):

$$N = k_1 R_d \rho + k_2' \frac{p_w}{T} Z_w^{-1} + k_3 \frac{p_w}{T^2} Z_w^{-1} \tag{2.7}$$

where ρ is the total density of dry gases and water vapour; R_d is the specific gas constant of the dry constituent ($R_d = R/M_d$, R is the universal gas constant and equals to 8314.4621 ± 0.0075 J/(kmol·K) (`http://physics.nist.gov/cuu/Constants/index.html`)); M_d is the molar mass of the dry gases and equals to 28.9644 ± 0.0014 kg/kmol (*Davis et al.*, 1985). The coefficient $k_2' = k_2 - (M_w/M_d)k_1$ and M_w is the molar mass of water vapour and equals to 18.0152 kg/kmol (*Davis et al.*, 1985). The values of k_1, k_2, k_3, and k_2' used in this thesis are summarized in Table 2.1. The first term of Equation (2.7) gives us the hydrostatic refractivity depending only on the total density and not on the wet/dry mixing ratio, while the second and third terms give us the wet refractivity. Combining Equation (2.7) and (2.5) gives the total delay, which consists of the hydrostatic and the wet delay:

$$\triangle L(\epsilon, \phi) = \triangle L_h(\epsilon, \phi) + \triangle L_w(\epsilon, \phi) \tag{2.8}$$

The hydrostatic delay is often referred to the zenith direction (denoted by $\triangle L_h^z$), defined as Zenith Hydrostatic Delay (ZHD), and can be obtained by applying the condition that hydrostatic equilibrium is satisfied (*Davis et al.*, 1985):

$$\frac{dp}{dh} = -\rho(h)g(h) \tag{2.9}$$

where g is the acceleration due to gravity at the vertical coordinate; p is the total pressure. Then the integration of the first term in Equation (2.7) gives:

$$\triangle L_h^z = \left(10^{-6} k_1 R_d g_m^{-1}\right) P_0 \tag{2.10}$$

where P_0 is the total ground pressure in hPa and g_m is given by:

$$g_m = \frac{\int_0^\infty \rho(h)\, g(h)\, d(h)}{\int_0^\infty \rho(h)\, d(h)} \tag{2.11}$$

The value of g_m is given by *Saastamoinen* (1972) referring to the acceleration gravity at the mass centre of a vertical column of the atmosphere:

$$g_m = (9.784 \pm 0.001\,\mathrm{m/s^2}) f(\lambda, H) \tag{2.12}$$

where

$$f(\lambda, H) = \left(1 - 2.66 \cdot 10^{-3} \cos(2\lambda) - 2.8 \cdot 10^{-7} H\right) \tag{2.13}$$

where λ and H are the site latitude in degrees and the height above the geoid in m, respectively.

If we input all the constants in Equation (2.10) along with their uncertainties (assumed uncorrelated), the expression of the ZHD is given by:

$$\triangle L_h^z = (2.2767 \pm 0.0015)\,\frac{P_0}{f(\lambda, H)} \tag{2.14}$$

where ZHD is in units of mm. The elevation dependence of the ZHD can de modelled using hydrostatic mapping functions (*Niell,* 1996 and *Boehm et al.,* 2006). The azimuth dependence of the ZHD will be discussed later when horizontal delay gradients are presented.

The wet delay can be obtained by integrating the second and third terms of Equation (2.7). Since the compressibility factor Z_w is very close to one, it can be ignored from the calculation giving an impact which is less than the uncertainty of the formula itself (*Rüeger*, 1999):

$$\triangle L_w(\epsilon, \phi) = 10^{-6} \int_S \left(k_2' \frac{p_w(s)}{T(s)} + k_3 \frac{p_w(s)}{T(s)^2} \right) ds \tag{2.15}$$

Equation (2.15) can be further modified by introducing a mean temperature T_m which is defined as:

$$\int_S \frac{p_w(s)}{T(s)}\, ds = T_m \int_S \frac{p_w(s)}{T(s)^2}\, ds \tag{2.16}$$

and becomes:

$$\triangle L_w(\epsilon, \phi) = 10^{-6} \left(k_2' + \frac{k_3}{T_m} \right) \int_S \frac{p_w(s)}{T(s)}\, ds \tag{2.17}$$

The slant wet delay can be converted to an equivalent Zenith Wet Delay (ZWD), denoted by $\triangle L_w^z$, using wet mapping functions (*Niell,* 1996 and *Boehm et al.,* 2006), and its azimuth dependence is described by the horizontal delay gradients (*Bar-Sever et al.*, 1998):

$$\triangle L_w(\epsilon, \phi) = m_w(\epsilon)\,(\triangle L_w^z + \cot(\epsilon)(G_n \cos(\phi) + G_e \sin(\phi))) \tag{2.18}$$

where $m_w(\epsilon)$ is the wet mapping function; G_n and G_e are the north and east horizontal delay gradients. Equation (2.18) can also be applied for the hydrostatic delay, but using a hydrostatic mapping function.

2.2.2 From wet delay to IWV

The IWV is related to the ZWD via a conversion factor Q:

$$V = \frac{\triangle L_w^z}{Q} \tag{2.19}$$

where Q can be derived using Equations (1.1), (1.2), and (2.17):

$$Q = 10^{-6}\,\rho_w\,R_w\left(k_2' + \frac{k_3}{T_m}\right) \tag{2.20}$$

where ρ_w is the density of liquid water; R_w is the specific gas constant for water vapour; k_3 and k_2' are same as defined in the previous section. The mean temperature T_m can be obtained using Numerical Weather Prediction (NWP) model output or reanalysis products (*Bevis et al.*, 1994; *Hagemann et al.*, 2003; and *Wang et al.*, 2005). One example of the time series of Q is shown in Figure 2.4, where the values were calculated at the Onsala Space Observatory using T_m obtained from the reanalysis product of the European Centre for Medium-Range Weather Forecasts (ECMWF). The uncertainty of Q is discussed in Section 3.2.

2.2.3 Water Vapour Radiometer

The atmospheric emission at microwave frequencies is mainly caused by water in the forms of liquid and vapour, and by oxygen. There is a water vapour spectral line at 22.235 GHz. The Water Vapour Radiometer (WVR) observes the sky emission at a frequency near this line which therefore can be used to infer the wet delay. The liquid water also emits radiation in the same frequency. Fortunately, due to the fact that the emission from the liquid water and water vapour have significant different spectral features, it is possible to separate their contributions by performing measurements at two different frequencies (*Elgered*, 1993).

The sky brightness temperature (T_{bf}) observed by a WVR given a certain frequency (f) can be expressed as:

$$T_{bf} = T_{bg}\,e^{-\tau(f)} + \int_0^\infty T(h)\,\alpha(f,h)\,e^{-\tau(f,h)}\,dh \tag{2.21}$$

where T_{bg} is the cosmic background temperature and approximately equals to 2.7 K; T is the physical temperature in K; α is the total attenuation due to water vapour, liquid water, and oxygen; and the atmospheric opacity (τ) is given by:

$$\tau = \int_0^\infty \alpha(h)\,dh \tag{2.22}$$

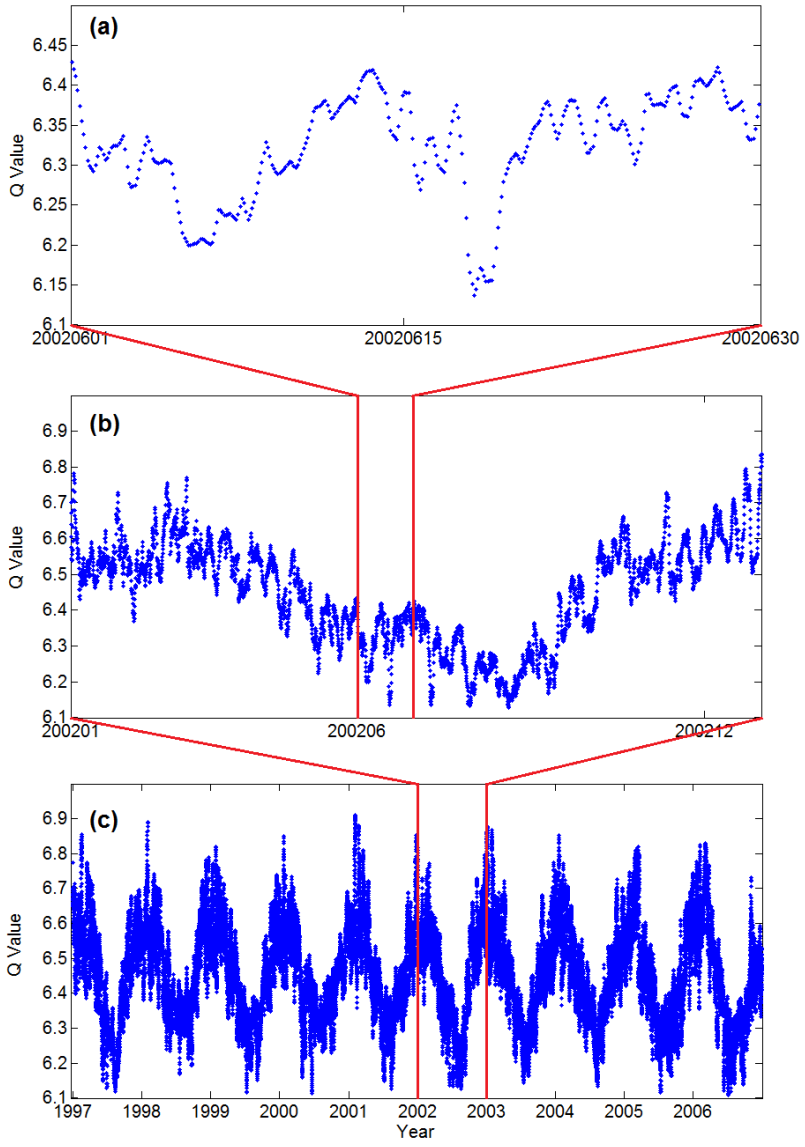

Figure 2.4: Time series of Q values calculated for the Onsala Space Observatory for (a) the month of June, 2002, (2) the year of 2002, and (c) the time period from January 1997 to December 2006.

Based on T_{bf} measured at two frequencies, the wet delay can be calculated (*Elgered*, 1993 and *Jarlemark*, 1994):

$$\triangle L_w = k \left[\left(\frac{f_1}{f_2} \right)^2 T'_{bf_1} - T'_{bf_2} - T_{c,ox} \right] \tag{2.23}$$

where T'_{bf_1} and T'_{bf_2} are linearized sky brightness temperatures; the value of the coefficient k is determined by the atmospheric pressure and temperature; and $T_{c,ox}$ in-

Figure 2.5: The WVR located at the Onsala Space Observatory.

cludes both the contribution from the cosmic background and from the oxygen (*Jarlemark*, 1997).

The WVR located at the Onsala Space Observatory (Figure 2.5) measures the sky emission at two frequencies (21.0 GHz and 31.4 GHz). Since 1992, it is operated continuously in a so called "sky-mapping" mode, which corresponds to a repeated cycle of approximately 60 observations spread over the sky with the lowest elevation angles of 20°, typically resulting in 6,000–9,000 measurements every day. The acquired data were analyzed using an in-house Matlab based software package to estimate the ZWD. Under this "sky-mapping" mode, the WVR results may also be used for characterization and modelling of the fluctuations of the wet delay (*Davis et al.*, 1993). These characterizations can lead a better selection of parameters for the stochastic filtering used in the processing of space geodetic data, such as GPS and VLBI. The formal uncertainty of the WVR-derived ZWD values is of the order of 0.5–3.0 mm. It is inferred from the misfit of the tip-curve calibrations, which are affected by atmospheric inhomogeneities. On the absolute scale, however, the uncertainty (one standard deviation) is of the order of 7 mm (around 1.1 kg/m^2 in IWV), assuming that the corresponding uncertainties in the observed sky brightness

temperatures are 1 K (*Elgered*, 1993).

Figure 2.6 depicts the IWV estimates and corresponding 1-σ accuracies (without consideration of the uncertainty in the observed sky brightness temperature) calculated from the ZWD, which were obtained using WVR observations acquired at the Onsala Space Observatory from January 1997 to December 2006. The used Q-values are shown in Figure 2.4. The WVR data were interpolated to a 2 h temporal resolution. The IWV time series is zoomed into one year and one month in order to illustrate the variation of the IWV. The data gaps in the time series are due to several repair and upgrade periods. Furthermore, data were removed due to the poor accuracy of the WVR measurements during rain when liquid water drops are not much smaller than the wavelength of the observed emission. This is realized by removing data when the inferred liquid water content is larger than 0.7 mm.

2.2.4 Very Long Baseline Interferometry

Very Long Baseline Interferometry (VLBI) acquires observations of the same radio source simultaneously by many telescopes, which are combined in order to result in a synthesized telescope with a size that equals to the maximum separation between the telescopes. In radio astronomy, the combined measurements are able to resolve the image of radio source with a much higher resolution (*Thompson et al.*, 2001). For geodetic applications (*Sovers et al.*, 1998), the differential time of arrival of the signal traveling from a radio source to a pair of telescopes is the most important parameter. Due to different locations of telescopes, the signal from the radio source will arrive to different telescopes at different time epochs. The time delay can be estimated by correlating the received signals with each other. The time delay is dependent on the separation of the pair of telescopes and on the position of the radio source relative to the baseline between the telescopes. Therefore, based on the time delays obtained from measurements by many telescopes and from different radio sources in different directions, when the Earth is rotating, some unknown parameters can be estimated, e.g. telescope positions, Earth rotation and orientation parameters, clock corrections, ZWD, and horizontal delay gradients.

The geodetic VLBI site at the Onsala Space Observatory has a 20 m telescope, which is covered by a radome (Figure 2.7). The Onsala VLBI site participates regularly in geodetic VLBI sessions which are usually 20 to 30 individual sessions each year (*Haas et al.*, 2003). Therefore, we cannot use VLBI observations for continuous monitoring of the IWV. In addition, there are less than 150 telescopes world-wide that have been and are used for geodetic VLBI and 90 % of them are located on the northern hemisphere. This indicates that the spatial resolution of the VLBI-derived IWV is also one of the disadvantages of the technique. However, since the antenna of the VLBI telescope has a very high directivity, it is less effected by signal multipath. Meanwhile, the VLBI technique has the advantage of high long-term stability due to

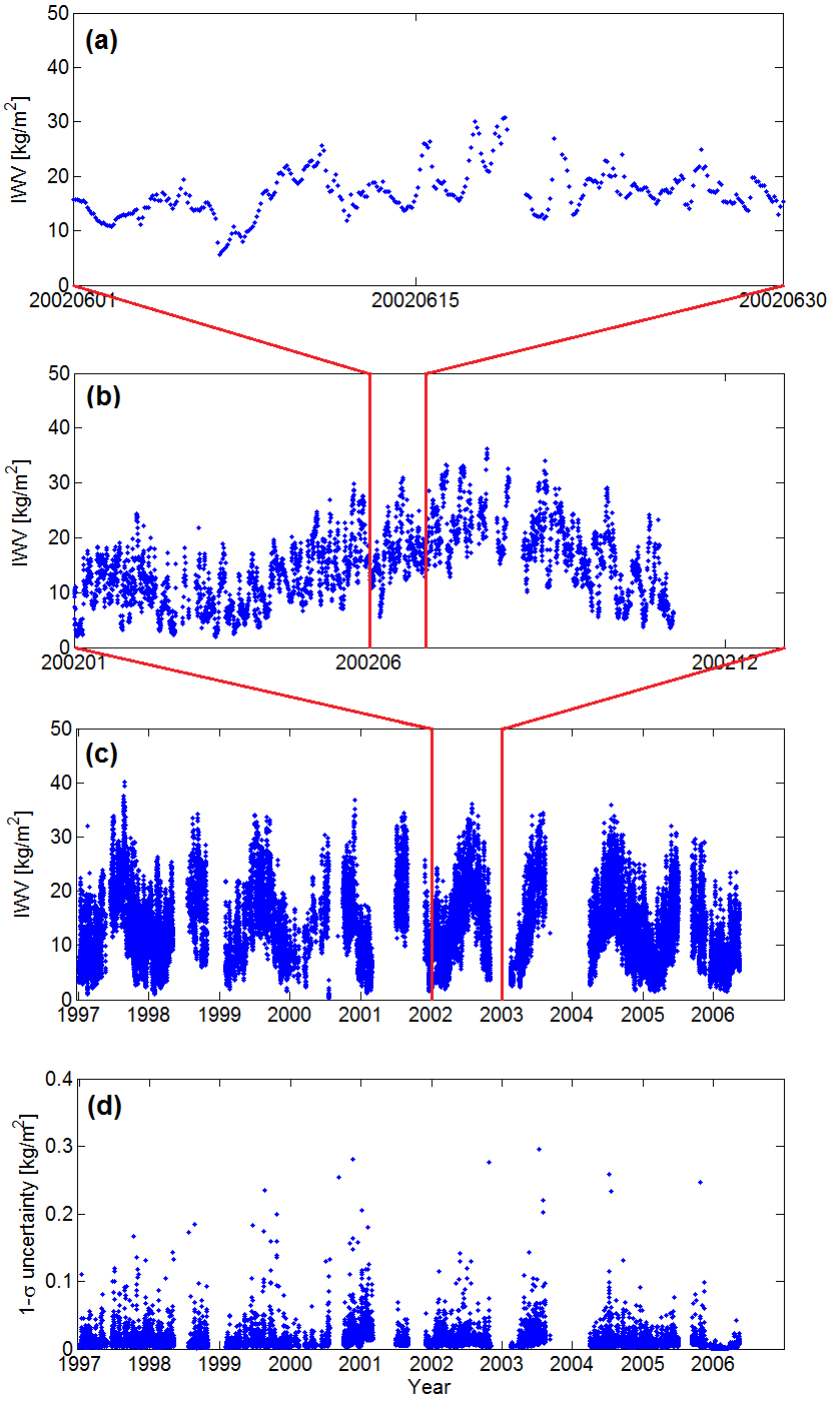

Figure 2.6: The IWV derived from observations acquired by the WVR at the Onsala Space Observatory shown for (a) the month of June, 2002, (b) the year of 2002, (c) the time period from January 1997 to December 2006, and (d) the 1-σ uncertainty for the corresponding time period.

Figure 2.7: The geodetic VLBI site using the 20 m telescope enclosed by the radome at the Onsala Space Observatory. The WVR is seen in the foreground.

its stable instrumentation. Given these advantages, the VLBI-derived IWV may be used as a reference for detecting systematic errors in the IWV obtained from other techniques (see Paper C).

Figure 2.8 depicts the time series of the IWV estimates and the corresponding 1-σ accuracies calculated from the VLBI ZWD (estimated for each 2 h), using the Q-value shown in Figure 2.4, at the Onsala Space Observatory. The detailed description of the data processing needed to infer the ZWD from the VLBI measurements is given in Paper A.

2.2.5 Global Positioning System

The Global Positioning System (GPS) is a satellite navigation system which can provide both position and time information. GPS is working under in principle all weather conditions and anywhere as long as there is an unobstructed line of sight to four or more GPS satellites. It is developed and maintained by the United States government and is freely accessible for civilian applications and scientific research.

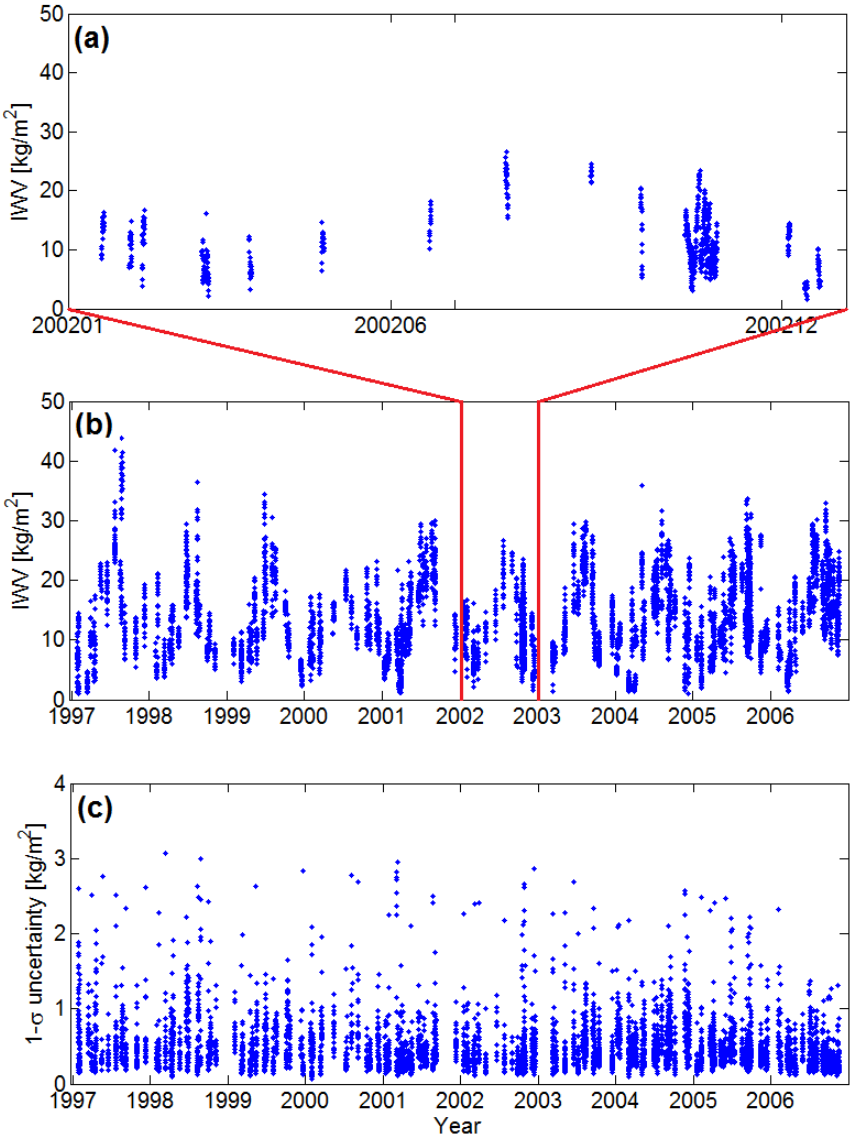

Figure 2.8: The IWV derived from the observations acquired for the VLBI site (Onsala) at the Onsala Space Observatory for (a) the year of 2002, (b) the time period from January 1997 to December 2006, and (c) the 1-σ uncertainty for the corresponding time period.

Since the first experimental Block-I GPS satellite was launched in 1978, GPS has been in operation for over 30 years. It consists of more than 30 satellites orbiting the Earth at an altitude close to 20,200 km (above the surface of the Earth), and in 6 nearly circular orbital planes with an inclination angle of 55°. With approximately 11 hours, 58 minutes of the orbital period, each satellite can make two revolutions in one sidereal day. Currently, GPS uses two frequencies 1.575 GHz (L1)

and 1.228 GHz (L2) to carry the signals. A third frequency 1.176 GHz (L5), which is proposed for use as a civilian Safety-of-Life (SoL) signal, is being implemented.

The fundamental observable of GPS is the signal propagation time from a satellite to a receiver. Multiplying the propagation time by the speed of light in vacuum gives the pseudorange between the satellite and the receiver. Note that the pseudorange is almost like a range, except that it includes additional effects, e.g. clock errors both from the satellite and the receiver. Two types of pseudoranges are obtained by correlating the code in the received signal (code measurements), or the carrier phase of the received signal (carrier phase measurements) to the replica from the receiver. Code measurements are normally used for navigation purposes giving an accuracy of a few metres. For applications demanding higher accuracies (centimetres or better), carrier phase measurements are necessary because the phase can be measured to 1 % of the wavelength of the carrier signal, which is around 2 mm for L1 and L2. A carrier phase measurement in units of length can be expressed as (*Teunissen and Kleusberg*, 1998)

$$\Phi = D + c\,(T_r - T_s) - \triangle I + \triangle L + \lambda N + \epsilon \tag{2.24}$$

where Φ is the carrier phase observable and D is the true distance between the satellite and the receiver; c is the speed of light in vacuum; T_r and T_s are the receiver and satellite clock offsets relative to the GPS time; $\triangle I$ is the ionospheric delay that presents itself as a phase advance; $\triangle L$ is the total delay in the neutral atmosphere; N is the integer number of cycles referred as the phase ambiguity which can be converted to length by multiplying by λ (the wavelength of the carrier frequency), and ϵ is the sum of other unmodelled errors, e.g. signal multipath, antenna phase centre variations, and radome effects.

In Equation (2.24), the clock error (T_r–T_s) can either be eliminated by using double difference techniques (*Blewitt*, 1993), or be estimated by using the Precise Point Position (PPP) method which processes data from one receiver at a time (*Zumberge et al.*, 1997). Due to a frequency dependence, the main contribution of the ionospheric delay (∼99.9 %) can be removed by forming the ionospheric free Linear Combination (LC) using two carrier phase measurements at two different frequencies (*Hernández-Pajares et al.*, 2007). The neutral atmospheric delay ($\triangle L$) can be estimated along with other unknown parameters. The phase ambiguity (N) is initially unknown. It however will be the same for a given satellite to a given receiver, as long as the receiver can keep tracking the satellite. Hence, it is constant as long as the receiver is phase locked on signals from the satellite. For unmodelled errors (ϵ), the antenna related errors (i.e. antenna phase centre variations and radome effects) can be significantly removed using calibration models in the data processing. However, signal multipath is difficult to model since it is highly coupled to the surrounding environment of the antenna. One method to reduce multipath impact is to implement microwave absorbing material below the antenna plane (see Paper B).

Figure 2.9: The GPS site (ONSA) located at the Onsala Space Observatory is a site in the International Global Navigation Satellite System (GNSS) Service (IGS), formerly the international GPS service, network (`http://igscb.jpl.nasa.gov/network/site/onsa.html`). The antenna is protected by a hemispheric radome and microwave absorbing material is attached to the antenna.

The total delay ($\triangle L$) due to the neutral atmosphere is normally referred to the Zenith Total Delay (ZTD), which is given by the sum of the ZHD and the ZWD. In this thesis, the ZTD was estimated by GIPSY/OASIS II v.5.0 (*Webb and Zumberge*, 1993) using the PPP strategy. The model for the ZTD consists of an a priori ZHD obtained using the model given by *Saastamoinen* (1973) (i.e. 2287 mm for the Onsala site shown in Figure 2.9) and an a priori ZWD (100 mm). Corrections to this a priori ZTD and the horizontal delay gradients were estimated using a random walk model. The ZHD was calculated from ground pressure using Equation (2.14) and subtracted from the ZTD to give the ZWD. A detailed discussion on the GPS data processing is given in Paper A.

The time series of the IWV calculated from the ZWD, using the Q-value shown in Figure 2.4, estimated for the Onsala GPS site (Figure 2.9) are shown in Fig-

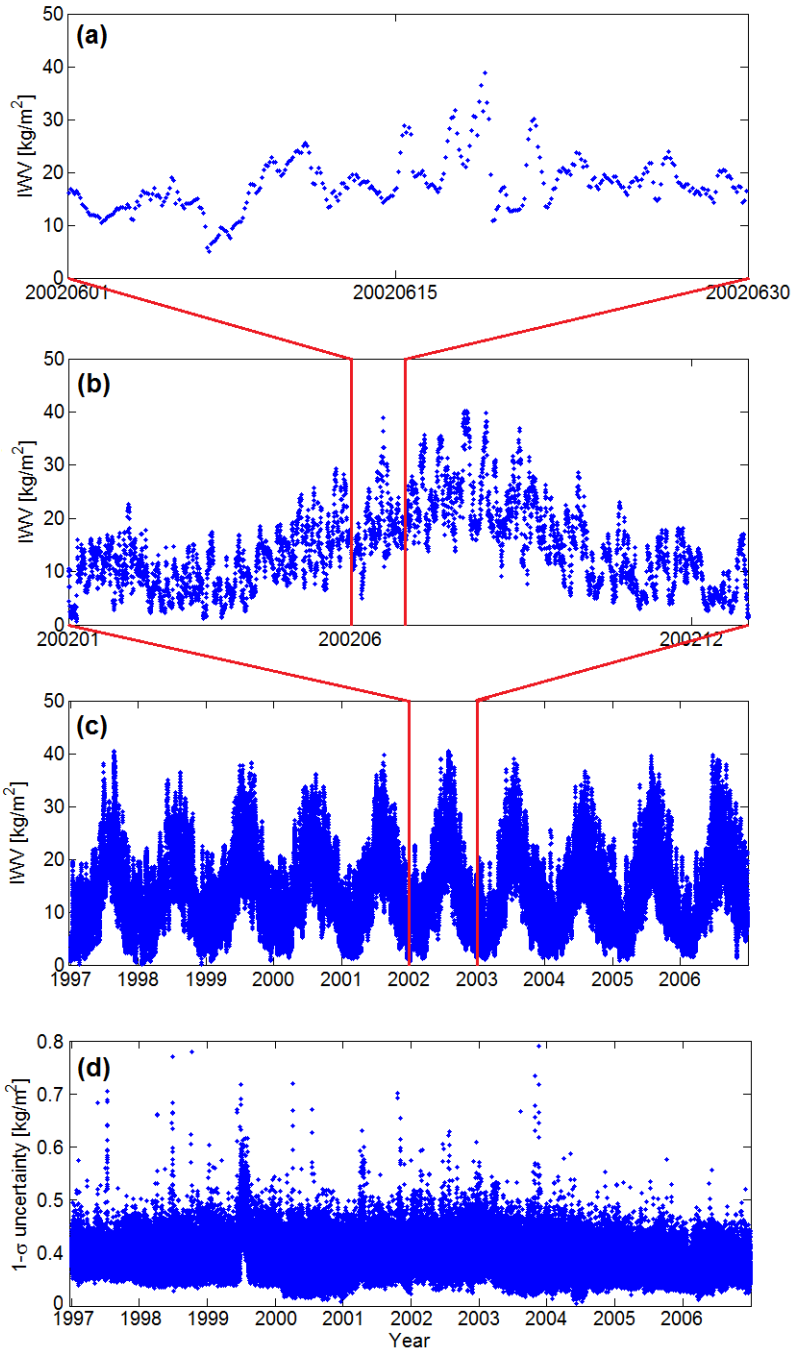

Figure 2.10: The IWV derived from the observations acquired at the GPS site (ONSA) at the Onsala Space Observatory shown for (a) the month of June, 2002, (b) the year of 2002, (c) the time period from January 1997 to December 2006, and (d) the 1-σ uncertainty for the corresponding time period.

ure 2.10. The GPS data were interpolated to a 2 h time interval from the original 5 min resolution. Note in Figure 2.10, the 1-σ uncertainty of the IWV was simply obtained by the formal error of the ZWD, given by the GIPSY processing, divided by Q. Therefore, no uncertainties due to the conversion, e.g. the error from the ground pressure and the mean temperature, were included. This is same for Figures 2.6 and 2.8. A detailed discussion on the uncertainty of the GPS-derived IWV is given in Section 3.2.

Because of the increasing number of applications, the reliable operation, and the continuous updating of the system, the number of continuously operating GPS ground sites keeps growing. For example, globally the number of sites from IGS is now (April 2012) over 360 (Figure 2.11a). Since April 2005, Denmark is hosting the EIG EUMETNET GNSS water vapour programme (E-GVAP) to provide EUMETNET members with water vapour estimates for operational meteorology in near real-time. Currently, the E-GVAP network consists of more than 1500 GNSS sites, which are mainly in Europe (Figure 2.11b). In Sweden, the national network of permanent reference sites for GPS (SWEPOS®, Figure 2.11c) has been in operation since 1993, used for land surveying and geophysical research (*Johansson et al.*, 2002). From 20 sites in the autumn of 1993, the total number of SWEPOS sites is now (April 2012) 274.

2.3 Summery of Paper A

The goal of Paper A is to assess the accuracy of the different techniques that can be used to infer the ZWD. The results from the comparisons of 10-year-long time series of the ZWD, estimated using GPS, geodetic VLBI, a WVR, radiosonde observations, and the reanalysis product of ECMWF are presented. In order to compare the data sets with each other, the different temporal resolutions of all ZWD time series were matched using a temporal filter. Comparisons between three co-located techniques (GPS, VLBI, and WVR) result in mean values of the ZWD differences at a level of a few millimetres and the standard deviation of less than 7 mm. The best agreement is seen in the GPS−VLBI comparison with a mean difference of −3.4 mm and a standard deviation of 5.1 mm. Comparisons of radiosonde-derived ZWD show larger scatter due to distance between the sites. A wet bias of up to 7 mm is obtained for the ECMWF reanalysis product with respect to other techniques. In addition, we find that the GPS−WVR comparison shows a much smaller seasonal variation in the monthly standard deviation of the ZWD difference than the GPS−RS and the GPS−ECMWF comparisons. It indicates that uncertainties of the ZWD inferred from the GPS and WVR data do not depend on the ZWD value.

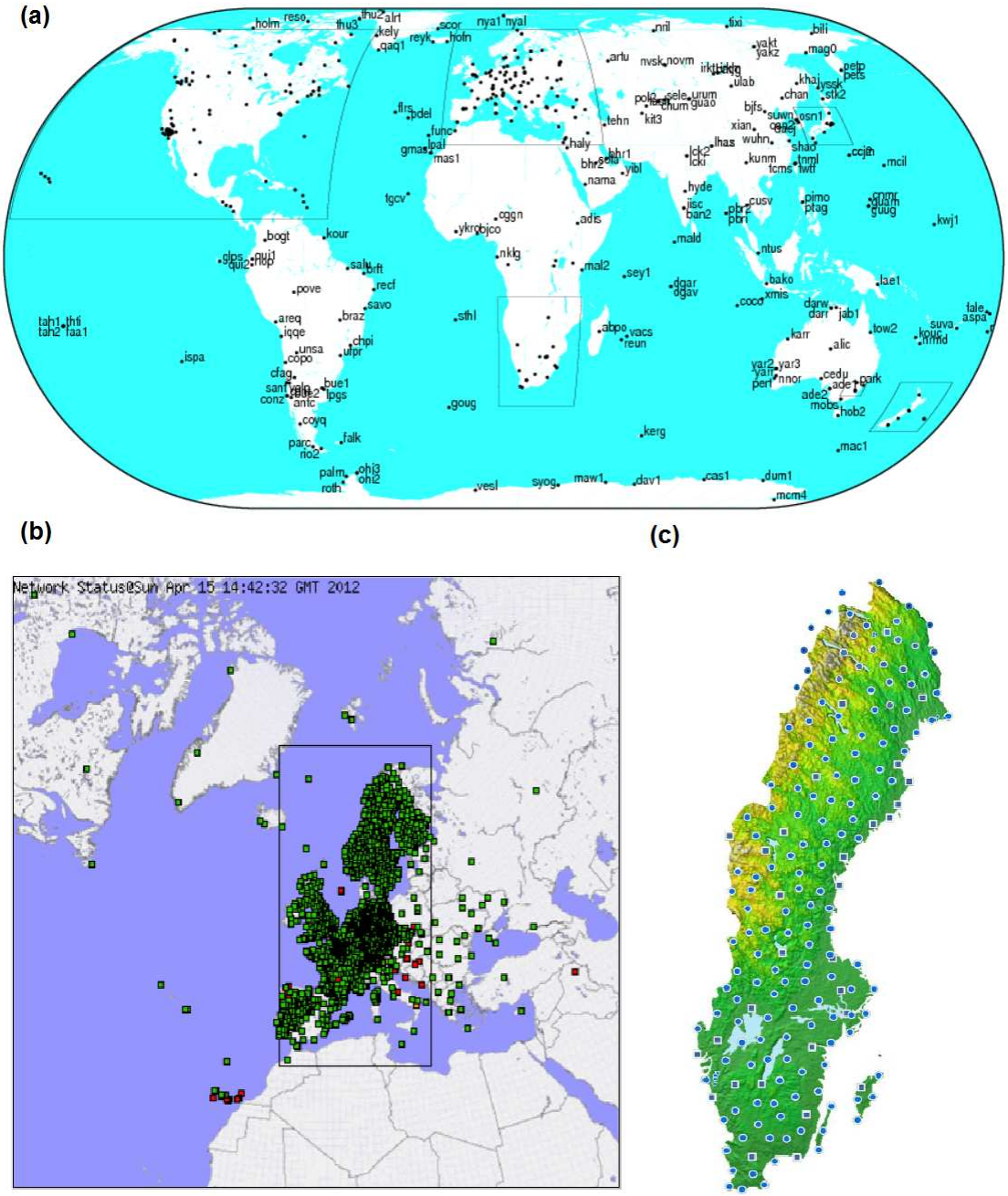

Figure 2.11: (a) The IGS global covered tracking network (source: `http://igscb.jpl.nasa.gov/network/complete.html`), (b) the map of the E-GVAP network with different color showing the status of the site (source: `http://egvap.dmi.dk/`), and (c) the SWEPOS network and a number of Norwegian and Finnish sites that are used in SWEPOS. Blue squares are sites of Class A type with geodetic quality. Blue dots are sites of Class B type, established for real time kinematic purposes (source: `http://www.clge.eu/documents/events/93/swepos.pdf`).

Chapter 3

Uncertainty Analysis of the IWV from GPS

All GPS measurements are subject to error sources that influence the uncertainty of the estimated ZWD. Additionally, the conversion from the ZWD to the IWV will also add uncertainties, e.g. due to imperfect determination of the ground pressure and the mean temperature of the atmosphere. All those uncertainties shall be included when we calculate the final uncertainty of the GPS-derived IWV.

Errors in GPS measurements can be random or systematic, or a mixture of the two, depending on the time scale studied. Random errors vary in an unpredictable way causing stochastic variations in GPS measurements. Since the expected (mean) value of random errors is zero, the impact of such error can be minimized as the number of measurements increases. Systematic errors tend to shift all GPS measurements in a systematic way introducing an non-zero offset between the measured value and expected (true) value, and cannot be averaged out as the length of measurements becomes longer. Systematic errors in GPS measurements can however change at a specific time epoch. For example, a change of the GPS antenna or an attachment of microwave absorbing material to the antenna may introduce such an offset. Systematic errors may also change slowly with time, e.g. the impact of signal multipath on a given GPS site varies due to growing vegetation in the area surrounding the site.

In order to interpret GPS measurements correctly and draw valid conclusions on the quality of the IWV estimates, the uncertainty of the GPS-derived IWV must be carefully evaluated and dealt with properly.

3.1 Statistical analysis

A statistical analysis can be used to evaluate the uncertainty of the GPS-derived IWV if independent estimates obtained from at least three co-located techniques,

measuring the same true variability of the atmospheric water vapour, are available. The Standard Deviation (SD) of the IWV difference between techniques A and B including N data points can be expressed as:

$$S_{A-B} = \sqrt{\frac{1}{N-1}\sum_{i=1}^{N}\left(V_{A(i)} - V_{B(i)} - \overline{V_A - V_B}\right)^2} \tag{3.1}$$

where the overline denotes the mean value of the difference. The individual IWV estimates from each technique have associated errors:

$$V_{A(i)} - \overline{V_A} = V_i - \overline{V} + E_{A(i)} \tag{3.2}$$
$$V_{B(i)} - \overline{V_B} = V_i - \overline{V} + E_{B(i)} \tag{3.3}$$

where V_i is the true value of IWV and E terms are the errors which have a zero mean. If we combine Equations (3.2) and (3.3), and input into Equation (3.1), we will have:

$$S_{A-B} = \sqrt{\frac{1}{N-1}\sum_{i=1}^{N}\left(E_{A(i)} - E_{B(i)}\right)^2} \tag{3.4}$$

If E_A and E_B are uncorrelated, Equation (3.4) becomes:

$$S_{A-B} \approx \sqrt{\overline{E_A^2} + \overline{E_B^2}} \tag{3.5}$$

where E terms can be solved by forming the equation above three times for pairwise comparisons from three techniques.

Since the E terms only address the random errors, in order to determine the total uncertainty of the IWV, caused by both random and systematic errors, the mean IWV difference (M_{A-B}) between two techniques is needed. M_{A-B} is determined by the possible biases in the IWV estimates for both techniques (B_A and B_B) and expressed as:

$$\begin{aligned} M_{A-B} &= \frac{1}{N}\sum_{i=1}^{N}\left(V_{A(i)} - V_{B(i)}\right) \\ &= \frac{1}{N}\sum_{i=1}^{N}\left(V_{(i)} + B_A - (V_{(i)} + B_B)\right) \\ &= B_A - B_B \end{aligned} \tag{3.6}$$

where the meaning of B_A and B_B is highly depending on the length of time scale studied. For a short time period where the length of measurements is not long

enough to average out random errors, the bias (B) is a mixture of random and systematic errors. For a longer time period giving a zero mean of random errors, the bias (B) is only caused by systematic errors.

As we can see from Equation (3.6), the bias of the IWV for one technique can only be obtained when it is compared to a technique with a known IWV bias or no bias at all, and for a long time period. After obtaining the values for E and B, the total uncertainty of the IWV can be calculated:

$$\sigma_V = \sqrt{\overline{E^2} + B^2} \tag{3.7}$$

One example of a statistical analysis can be found in Paper A. We presented the results from comparisons of 10-year-long time series of ZWD, estimated using GPS, geodetic VLBI, and a WVR. The three techniques are co-located at Onsala Space Observatory with a horizontal distance shorter than 100 m. Since the VLBI antenna has a very high directivity, the VLBI-derived ZWD is much less effected by signal multipath. Meanwhile, there was no instrument changes occurring on the Onsala VLBI antenna for the last 30 years. Therefore, the VLBI-derived ZWD for the 10-year-long time period can be considered as having only a small bias. Using Equations from (3.5) to (3.7), we calculated the total uncertainties in the ZWD and in the corresponding IWV, for each technique after assuming a bias of $+2$ mm, 0 mm and -2 mm in the VLBI-derived ZWD. The results are summarized in Table 3.1.

3.2 Theoretical analysis

A statistical analysis requires several independent techniques observing the atmospheric water vapour at the same location and at the same time. This method is difficult to apply for the IWV estimates obtained from a globally distributed GPS network. Therefore, a theoretical analysis is desired, where the total uncertainty of the GPS-derived IWV (σ_V) is calculated from independent sources of uncertainties associated with the input variables according to the rule of uncertainty propagation for uncorrelated input quantities. The equation used for a theoretical analysis was presented by *Immler et al.* (2010):

$$\sigma_V = \sqrt{\sum_{i=1}^{M} \left(\frac{\partial f(v_1, ..., v_M)}{\partial v_i} \sigma_i \right)^2} \tag{3.8}$$

where $f(v_1,...,v_M)$ is the functional relationship between the GPS-derived IWV and the input variables; σ_i is the uncertainty of the corresponding variable.

The GPS-derived IWV is converted from the ZWD via the conversion factor Q using Equation (2.19) where the ZWD is given by the subtraction of the ZHD from

Table 3.1: Calculated ZWD and corresponding IWV uncertainties given by a statistical analysis

	Standard deviation[a] [mm]			Mean difference[a] [mm]			E_{ZWD}[b]	B_{ZWD}[c]	σ_{ZWD}[d]	σ_{V1}[e]	σ_{V2}[f]
	GPS	VLBI	WVR	GPS	VLBI	WVR	[mm]	[mm]	[mm]	[kg/m^2]	[kg/m^2]
GPS	–	5.2	6.5	–	−3.1	−0.6	3.2	−1.1	3.4	0.52	0.53
VLBI	5.2	–	7.0	3.1	–	2.5	4.1	**2.0**[g]	4.6	0.71	0.72
WVR	6.5	7.0	–	0.6	−2.5	–	5.7	−0.5	5.7	0.88	0.89
GPS	–	5.2	6.5	–	−3.1	−0.6	3.2	−3.1	4.5	0.69	0.70
VLBI	5.2	–	7.0	3.1	–	2.5	4.1	**0.0**[g]	4.1	0.63	0.64
WVR	6.5	7.0	–	0.6	−2.5	–	5.7	−2.5	6.2	0.95	0.96
GPS	–	5.2	6.5	–	−3.1	−0.6	3.2	−5.1	6.0	0.90	0.91
VLBI	5.2	–	7.0	3.1	–	2.5	4.1	**−2.0**[g]	4.6	0.71	0.72
WVR	6.5	7.0	–	0.6	−2.5	–	5.7	−4.5	7.3	1.12	1.12

[a]The corresponding values were taken from Table 2 (synchronization to all data) in Paper A.
[b]The uncertainty of the ZWD only addressing the random errors.
[c]The bias in the ZWD estimates for each technique.
[d]The total uncertainty of the ZWD addressing both the random and systematic errors.
[e]The uncertainty of the IWV given by dividing σ_{ZWD} by 6.5 (a mean value of the conversion fact Q for the Onsala Space Observatory). The uncertainty of Q was not considered.
[f]The uncertainty of the IWV calculated using a similar way as σ_{V1}, but taking the uncertainty of 0.1 kg/m^2 for Q, which is taken from Table 3.4 for the MEDI site, into account ($\sigma_{V2}=\sqrt{\sigma_{V1}^2+0.1^2}$). The uncertainty of the ground pressure is insignificant since the ground measurements were used.
[g]Assumed values in order to relate the comparisons to an absolute scale.

the ZTD (denoted as $\triangle L^z$):

$$\triangle L_w^z = \triangle L^z - \triangle L_h^z \tag{3.9}$$

Combination of Equations (2.19) and (3.9) gives the functional relationship:

$$V = \frac{\triangle L^z - \triangle L_h^z}{Q} \tag{3.10}$$

Inputting Equation (3.10) into Equation (3.8) gives the expression for the propagation of the uncertainties from different sources to the total IWV uncertainty:

$$\sigma_V = \sqrt{\left(\frac{\sigma_{ZTD}}{Q}\right)^2 + \left(\frac{\sigma_{ZHD}}{Q}\right)^2 + \left(V\,\frac{\sigma_Q}{Q}\right)^2} \tag{3.11}$$

In order to calculate σ_V, we first need to study and determine values for σ_{ZTD}, σ_{ZHD}, and σ_Q.

3.2.1 Error budget of the GPS-derived ZTD

Ionospheric delay

Due to ionizing radiation, the Earth's ionosphere contains electrons in sufficient quantities to significantly delay the propagation of GPS signals. The ionospheric delay is dependent on the total amount of free electrons along the propagation path, named Total Electron Content (TEC), and the carrier frequency of GPS signals (*Klobuchar*, 1978). Normally, in order to remove the ionospheric impact, a ionosphere-free linear combination is used:

$$\Phi_{ion\_free} = \frac{f_1^2}{f_1^2 - f_2^2}\Phi_1 - \frac{f_2^2}{f_1^2 - f_2^2}\Phi_2 \tag{3.12}$$

where Φ_1 and Φ_2 are carrier phase measurements from two different frequencies (L1 and L2). Since this virtual measurement can only eliminate the ionospheric delay to the first order ($\sim$99.9 % of the total delay), smaller contributions from higher order terms remain, which however have more dramatic impact during strong solar activities, e.g. ionospheric storms (*Pireaux et al.*, 2010).

Fritsche et al. (2005) carried out an investigation on the impact of including corrections of the ionospheric delay for higher-order terms on GPS estimates using a global network, and with a focus on the last solar maximum (2001–2003). They found a linear dependency between the difference in the estimated vertical position and the peak electron densities (varying approximately from 2 mm to 12 mm when the daily means of the TEC unit increase from 25 to 175) when no corrections were applied for 2nd and 3rd-order terms. If we approximate the ZTD difference as

a factor of three smaller than the vertical position difference (*Hill et al.*, 2009), the corresponding ZTD difference would be from 0.6 mm to 4 mm. This is consistent to the result reported by *Fritsche et al.* (2005) where a ∼2 mm difference in the ZTD were observed when the TEC unit reaches 150. A similar study was performed by *Petrie et al.* (2010) but for a longer time period from 1995 to 2008. Using approximately 60 globally distributed GPS sites, they found that the mean difference in the vertical component, after applying 2nd and 3rd-order terms, was in a range from −0.3 mm to 0.5 mm for individual sites with minimum 10 year's data.

Satellite orbits

Errors in the estimates of the satellite coordinates will propagate directly to the estimates of the GPS parameters. If we use the PPP strategy to process the data obtained from a permanent GPS site where the site coordinates are usually kept fixed (one estimate per day), eliminate the ionosphere delay for the first order, and use the final IGS clock product, the impact of orbit errors on the estimated ZTD can be presented in a simplified analytical expression (*Douša*, 2010):

$$\frac{1}{\cos z_A^i}\sigma_{ZTD} = \cos \Psi_A^i \sigma_{X_{Rad}^i} + \sin \Psi_A^i \sigma_{X_{Tan}^i} \tag{3.13}$$

with

$$\Psi_A^i = \arcsin(\sin z_A^i R_A / R^i) \tag{3.14}$$

where z_A^i is the zenith angle seen from the ground receiver A to the satellite i; R_A and R^i are the distances from the top of the receiver to the geocentre, and the geometrical distance from the satellite to the geocentre, respectively; $\sigma_{X_{Rad}^i}$ and $\sigma_{X_{Tan}^i}$ are the radial and the tangential (along-track + cross-track) orbit errors. Based on Equation (3.13), Figure 3.1 depicts the impact of different components of the orbit errors on the estimated ZTD as the function of zenith angle. It is evident that the radial orbit error dominates the resulting ZTD error and the maximum impact factor of 1 is seen when the satellite is in the zenith direction. The maximum impact factor of the tangential orbit errors (0.13) is observed at a zenith angle of 45°. Figure 3.1 also indicts that it is difficult to give a general value to the uncertainty of the ZTD associated to the orbit errors due to the fact that different satellite constellations are seen from different GPS sites.

Nowadays, five GPS satellite orbit products are provided by IGS with the highest accuracy of about 2.5 cm (1D mean Root-Mean-Square (RMS) values over the three XYZ geocentric components) for the final orbit products with a 12–18 days latency. Table 3.2 presents the orbit accuracy for each component using the IGS reprocessed orbit product, which should be comparable to the operational final orbits. The mean and standard deviation were calculated based on satellite position repeatability for each pair of consecutive days. The tangential orbit errors are around 72 % larger than the radial error.

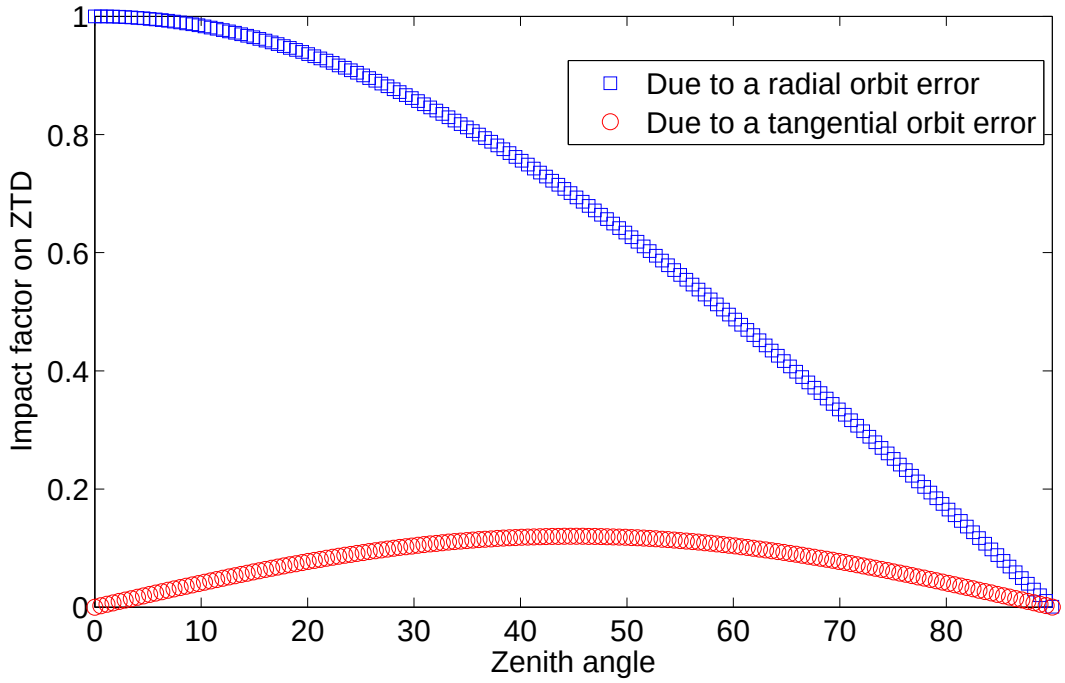

Figure 3.1: The impact factor of the radial and the tangential orbit errors on the estimated ZTD.

Table 3.2: Accuracy of IGS reprocessed orbits[a]

	Along Track [mm]	Cross Track [mm]	Radial [mm]
Mean	−0.3	−1.7	0.6
Standard deviation	36.8	38.6	21.3

[a]The table was taken from `http://igscb.jpl.nasa.gov/mail/igsmail/2010/msg00001.html`.

Signal multipath

The impact of signal multipath can be investigated using two co-located GPS sites, where the multipath effects should be considered as the major effects causing the difference in the estimated ZTD between the two sites. Paper B carried out such an investigation using two GPS sites at Onsala Space Observatory with a 12 m baseline. Using nearly 80 days of GPS data we found a mean RMS difference of ∼0.7 mm in IWV (corresponding to ∼4.5 mm in ZTD) caused by multipath effects. Such difference can be significantly reduced by using microwave absorbing material,

e.g. ECCOSORB®, attached below the antenna plane.

It should be noted that the results presented in Paper B cannot be applied globally since signal multipath is highly dependent on the local environment, which varies in time due to surrounding changes, e.g. different soil moisture (*Larson et al.*, 2010) and vegetation growing (*Granström and Johansson*, 2005). An example is shown in Figure 3.2 which depicts the carrier phase postfit residuals from the Onsala GPS site for March, April, May, and June 2010 in a polar plot. It is evident that larger residuals (for March and April) are observed at the area towards the west, which was covered by many trees. During the month of May, those trees were cut and the residuals (for May and June) from same area are now much smaller.

Antenna related errors

In order to obtain the highest accuracy in ZTD estimates, antenna related errors, i.e. Phase Centre Variations (PCV) and radome effects, need to be removed. Therefore, the absolute calibration of PCV for all the GPS satellite transmit antennas and the ground antenna (*Schmid et al.*, 2007) is necessary to be implemented in the data processing. The difference in the ZTD estimated with and without applying the PCV correction can vary from 2 mm to 10 mm (*Byun and Bar-Sever*, 2008 and *Thomas et al.*, 2011).

To avoid the accumulation of snow and for a general protection, many GPS antennas are equipped with radomes. Different shapes of radomes yield different impacts on the phase of the GPS signal. *Emardson et al.* (2000) found that the IWV offset introduced by a conical radome can be up to 1 mm (about 6.5 mm in ZTD). A smaller impact (less than 2 mm in ZTD) was observed from the use of a hemispheric radome (see Paper B). Given that many different radome types are used globally, applying a radome calibration in the data processing is necessary. Meanwhile, for the application of climate monitoring/research, changes should be avoided and during all circumstances be well documented.

Mapping functions

In GPS data processing, the slant path delay is converted to the equivalent ZTD (sum of the ZHD and the ZWD) using hydrostatic and wet Mapping Functions (MFs):

$$\triangle L = m_h(\epsilon) \cdot \triangle L_h^z + m_w(\epsilon) \cdot \triangle L_w^z \tag{3.15}$$

where ϵ is the elevation angle seen from the ground receiver to the satellite. *Stoew et al.* (2007) evaluated the accuracy of the New Mapping Functions (NMF) (*Niell*, 1996) and Improved Mapping Functions (IMF) (*Niell*, 2000) using ray tracing of radiosonde data. The resulting mean (M) and standard deviation (σ) of the slant

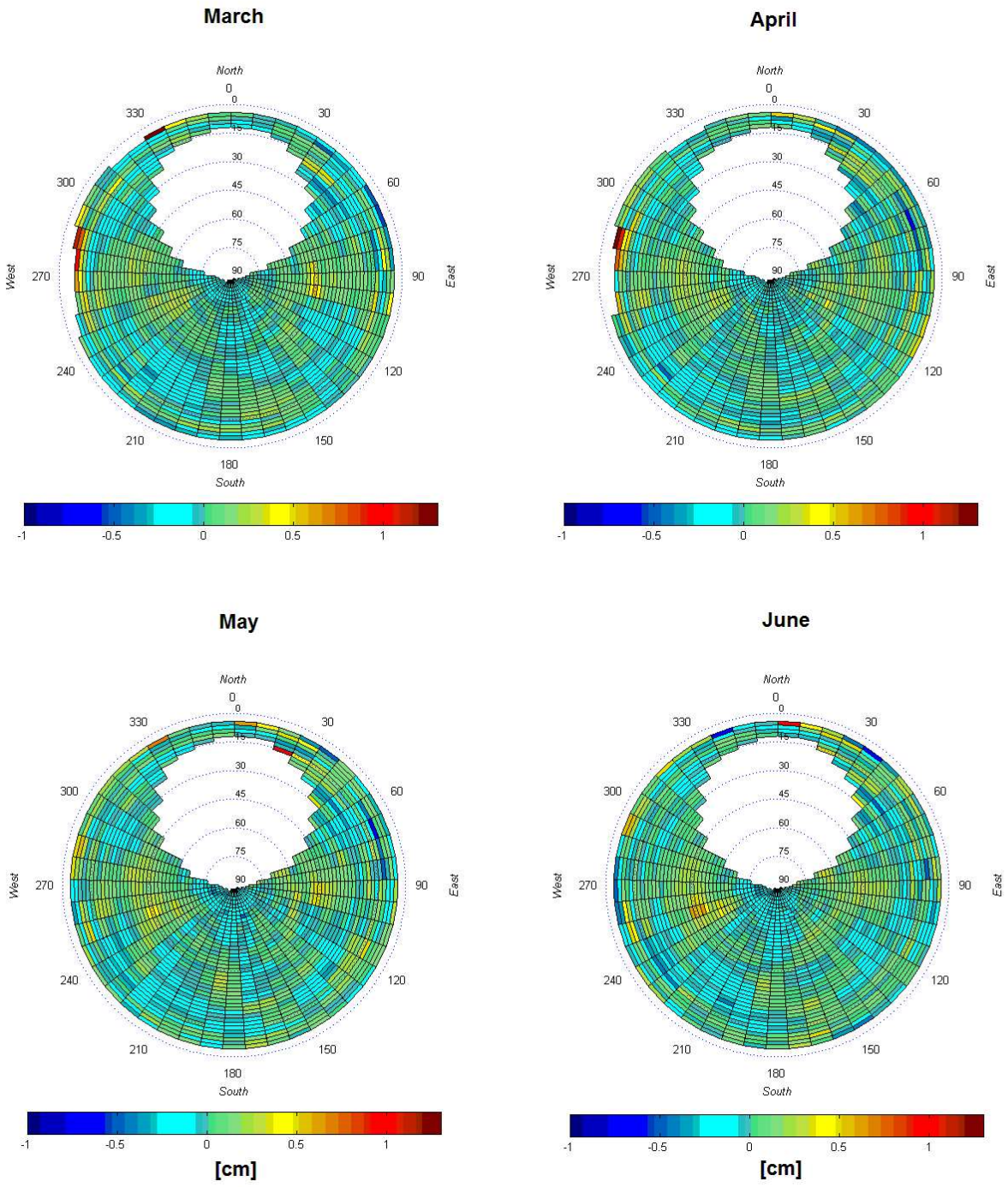

Figure 3.2: The carrier phase postfit residuals from the Onsala GPS site for March, April, May, and June 2010. Note the improvement at low elevations towards the west for May and June.

Table 3.3: Mean (M) and standard deviation (σ) of the slant delay errors[a]

	NMF_h		NMF_w		IMF_h		IMF_w	
Elevation angle	M [mm]	σ [mm]	M [mm]	σ [mm]	M [mm]	σ [mm]	M [mm]	σ [mm]
5°	10.6	24.87	−3.3	3.91	1.0	13.68	−2.5	1.87
7°	3.5	9.60	−1.0	1.20	0.4	4.50	−0.8	0.65
10°	0.7	2.30	−0.2	0.21	0.1	0.85	−0.1	0.13
15°	0.0	0.21	−0.0	0.01	0.0	0.05	−0.0	0.00

[a]Corresponding values for M_0, σ_0, ϵ_M, and ϵ_σ used in Equations (3.16) and (3.17) were taken from Table 1 in *Stoew et al.* (2007).

delay errors were modeled by:

$$M(\epsilon) = M_0 \cdot e^{-\epsilon/\epsilon_M} \tag{3.16}$$

$$\sigma(\epsilon) = \sigma_0 \cdot e^{-\epsilon/\epsilon_\sigma} \tag{3.17}$$

Values calculated from Equations (3.16) and (3.17) for four elevation angles (5°; 7°; 10°; 15°) are summarized in Table 3.3. It is clear that the accuracy of MFs is highly elevation dependent and the MF induced errors on slant delays are insignificant when the elevation angle is getting larger.

Summary of the ZTD uncertainty

Since there is no unique method to combine all error sources to calculate the uncertainty of the GPS-derived ZTD, we simply take the claimed 1-σ uncertainty (4 mm) from the IGS ZTD product as a lower threshold value. This accuracy can only be achieved if the following conditions are fulfilled:

- If corrections of the ionospheric delay for 2nd and 3rd-order are not applied, measurements acquired during strong solar activities should not be used in the data processing.

- Use final orbit/clock products from IGS or equivalent.

- Both absolute antenna PCV and radome calibrations need to be implemented.

- The signal multipath effects need to be minimized either by implementing microwave absorbing material to the antenna, or by locating the GPS antenna in an empty place. The impact of multipath effects would be smaller if we use high elevation cutoff angles, which however will degrade the geometry and increase the formal error of the ZTD estimate. Nevertheless, this may still be desired, e.g. for applications where long-term trends are estimated, and the formal error is not the limiting factor (see Paper C).

- An elevation cutoff angle of 10° or larger is recommended in order to minimize the impact of MFs.

3.2.2 Uncertainty of the ZHD

The ZHD for a given GPS site can be calculated using the ground pressure (Equations (2.14)). The variation of $f(\lambda, H)$, for different latitudes and different site heights, are shown in Figure 3.3. Since the impact of the uncertainties in the latitude and the height is negligible, the uncertainty of the ZHD is mainly determined by the uncertainty of the ground pressure (σ_{P_0}) and the uncertainty of the constant (σ_c). Using Equation (3.8), we have the uncertainty of the ZHD in mm:

$$\sigma_{ZHD} = \sqrt{\left(\frac{2.2767\,\sigma_{P_0}}{f(\lambda, H)}\right)^2 + \left(\frac{P_0\,\sigma_c}{f(\lambda, H)}\right)^2} \tag{3.18}$$

where σ_c equals to 0.0015.

Since not all GPS sites are equipped with barometers, direct pressure measurements are not always available. The uncertainty of the ground pressure obtained

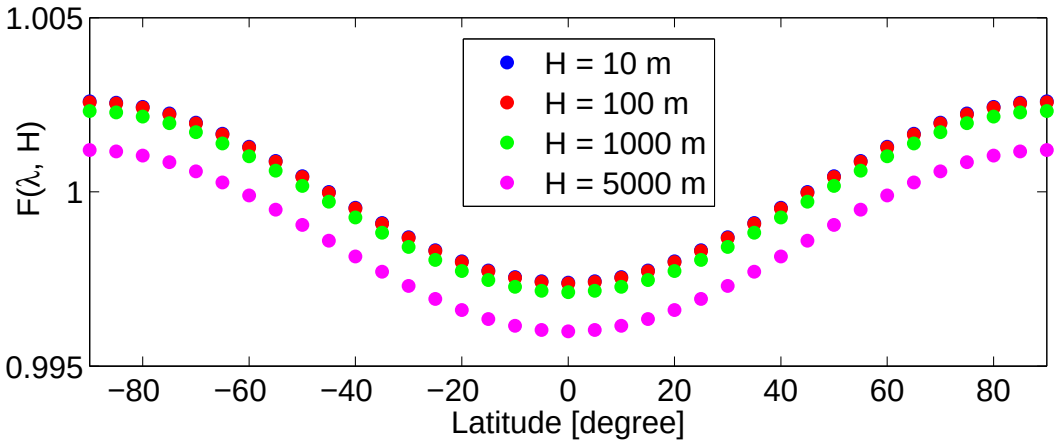

Figure 3.3: Values of $f(\lambda, H)$ calculated from different latitudes and from four different site heights.

from other methods was investigated by many studies. *Wang et al.* (2007) found an averaged RMS difference of 1.7 hPa given by comparisons between the ground pressure interpolated, both spatially and temporally, from nearby surface synoptic observations and local ground measurements at globally distributed 48 GPS sites covering a 8 year time period. Similar comparisons were carried out by *Heise et al.* (2009), but using the interpolated ground pressure from the ECMWF meteorological analysis at more than 60 global GPS sites. Using 1 year of data, they obtained a better agreement with an overall mean bias and a standard deviation of 0.0 hPa and 0.9 hPa, respectively. We did a similar test, but only for the GPS site at the Onsala Space Observatory, using over 10 years of data. The result shows a mean bias and a standard deviation of 0.1 hPa and 0.6 hPa, respectively.

3.2.3 Uncertainty of the conversion factor Q

The conversion factor Q is defined by Equation (2.20) where the uncertainties of the density of liquid water (ρ_w) and the specific gas constant for water vapour (R_w) are 0.002 kg/m^3 and 0.008 J/(kg·K), respectively (see text in Section 1.2). Since the impact of the uncertainties from these two parameters is insignificant (less than 0.1 % of the total Q uncertainty), the uncertainty of Q is mainly determined by the uncertainties in T_m, k_3, and k_2'. Implementing Equation (2.20) to Equation (3.8) gives:

$$\sigma_Q = 10^{-6}\,\rho_w\,R_w\sqrt{\left(\frac{\sigma_{k_3}}{T_m}\right)^2+\sigma_{k_2'}^2+\left(k_3\,\frac{\sigma_{T_m}}{T_m^2}\right)^2} \tag{3.19}$$

In order to evaluate the impact of the uncertainty in each variable on the total uncertainty of Q, we need to specify values and uncertainties for the constants k_3 and k_2', which are presented in Table 2.1. Figure 3.4 depicts the uncertainty of Q as a function of the uncertainty in T_m assuming that the value of T_m is 279 K (taken from Table 3.4 for the MEDI site). Three groups of values were used for the uncertainties of the constants k_3 and k_2', the nominal value (see Table 2.1), the double of the value and the half of the value. It is evident that when the uncertainty of T_m is sufficiently large, it tends to dominate the uncertainty of Q. Furthermore, the uncertainty of k_3 has a larger impact compared to the uncertainty of k_2'.

As shown in Equation (2.16), T_m can be calculated from vertical profiles of water vapour pressure (p_w) and physical temperature (T). If a GPS site is co-located with a radiosonde site, the profiles can be obtained from radiosonde measurements. Otherwise, globally they are usually derived from Numerical Weather Prediction (NWP) analyses. An RMS difference of 1.3 K in T_m was claimed by *Wang et al.* (2005) based on global comparisons between the NCEP/NCAR reanalysis and the radiosonde measurements using 6 years of data (NCEP=National Centers for Environmental Prediction of the US weather service; NCAR=National Center for At-

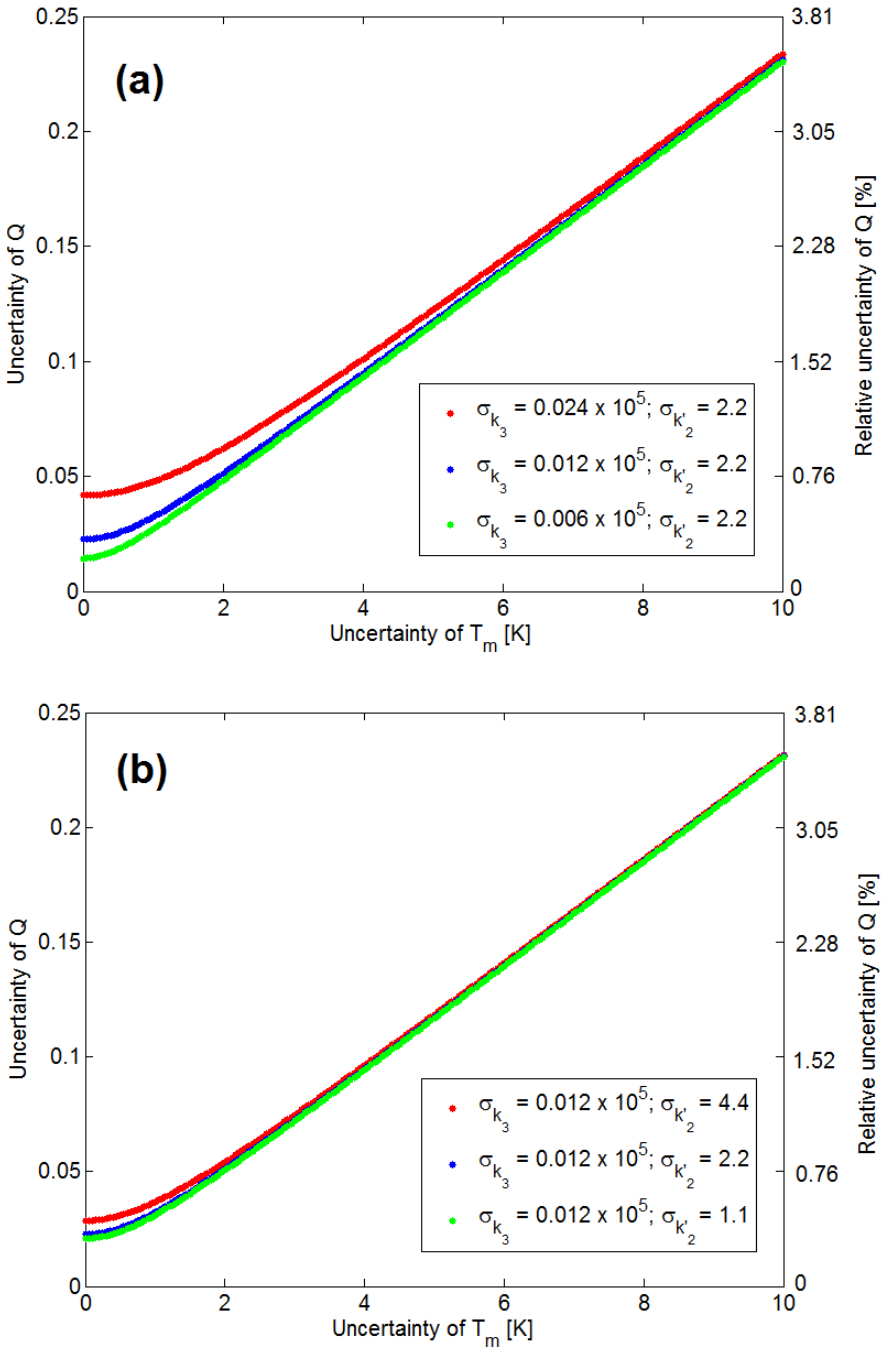

Figure 3.4: The uncertainty of the conversion factor Q as a function of the uncertainty in the mean temperature (T_m) and for three groups of the uncertainties in the constants k_3 and k_2', the nominal value (blue line), the double of the value (red line), and the half of the value (green line) for (a) a fixed uncertainty of k_2' and (b) a fixed uncertainty of k_3.

mospheric Research). T_m can also be calculated using a linear relation with surface temperature (T_s) (*Bevis et al.*, 1992):

$$T_m = 70.2 + 0.72\,T_s \tag{3.20}$$

This approach however shows a low accuracy in T_m at middle and high latitudes (T_m overestimated up to 5 K) and at low latitudes (T_m underestimated up to 6 K) (*Wang et al.*, 2005).

3.2.4 Summary of the uncertainty of the GPS-derived IWV

Now we can calculate the total uncertainty of the GPS-derived IWV after substituting Equations (3.18) and (3.19) to Equation (3.11):

$$\sigma_V = \sqrt{\left(\frac{\sigma_{ZTD}}{Q}\right)^2 + \left(\frac{2.2767\,\sigma_{P_0}}{f(\lambda,H)Q}\right)^2 + \left(\frac{P_0\,\sigma_c}{f(\lambda,H)Q}\right)^2 + \left(V\,\frac{\sigma_Q}{Q}\right)^2} \tag{3.21}$$

where σ_Q is given by Equation (3.19).

Table 3.4 summarizes the calculated total uncertainties of the GPS-derived IWV for three sites: COCO (96.8 °E, −12.2 °N), MEDI (11.7 °E, 44.5 °N), and EURK (−85.9 °E, 80.0 °N) representing different climates: moist, average, and dry. The heights above the mean sea level for the three sites are 4 m, 9 m, and 17 m, respectively. The corresponding absolute values for IWV, ZTD, ground pressure, and mean temperature were given using the mean values of the data from the year of 2004 for each site and obtained from the NCAR global, 2-hourly ground-based GPS IWV data set (*Wang et al.*, 2007). The values of the conversion factor Q were calculated using Equation (2.20).

As shown in Table 3.4, the uncertainties in the ZTD and the ZHD dominate the error budget of the resulting IWV contributing with over 94 % of the total IWV uncertainty. The impact of the uncertainty associated with the conversion factor Q is relative to the amount of water vapour and increases slightly when the weather conditions are getting moist.

3.3 Summary of Paper B

At the Onsala Space Observatory on the west coast of Sweden, an experimental pillar was constructed for flexible mounting of GPS antennas (see Figure 3.5). A 3-dimensional positioning adjustment was mounted below the antenna. Hence the antenna can be moved in different directions with respect to the radome and the pillar. Meanwhile, an arrangement was implemented to be able to move the radome up or down relative to the pillar. GPS observations were obtained with different

Table 3.4: Uncertainties in the GPS-derived IWV calculated from the uncertainties associated with input variables

Input variable	COCO	MEDI	EURK	Uncertainty	Corresponding IWV uncertainty								
					COCO			MEDI			EURK		
					[kg/m^2]	[%]	[%][i]	[kg/m^2]	[%]	[%][i]	[kg/m^2]	[%]	[%][i]
ZTD [mm]	2556	2445	2335	4[a]	0.66	1.6	47.2	0.64	2.9	48.5	0.59	11.8	49.5
Ground pressure P_0 [hPa]	1012.1	1012.2	1010.9	1.7[b]	0.62	1.5	40.8	0.60	2.7	42.6	0.55	11.0	43.1
				0.9[c]	0.33	0.8		0.32	1.5		0.29	5.8	
Constant[j]	2.2767	2.2767	2.2767	0.0015	0.25	0.6	6.5	0.24	1.0	6.8	0.22	4.0	6.9
Mean temperature T_m [K]	287.8	279.0	257.1	1.3[d]	0.18	0.4	3.3	0.10	0.5	1.3	0.02	0.4	0.2
				1.1[e]	0.15	0.4		0.09	0.4		0.02	0.4	
k_2' [K/hPa]	22.1	22.1	22.1	2.2[f]	0.07	0.2	0.5	0.04	0.2	0.2	0.01	0.2	0.1
k_3 [$10^5 \times$K^2/hPa]	3.739	3.739	3.739	0.012[f]	0.13	0.3	1.7	0.07	0.3	0.6	0.02	0.4	0.2
IWV [kg/m^2]	41	22	5										
Conversion factor Q	6.1	6.3	6.8										
Total IWV uncertainty (1)[g]					0.97	2.4		0.92	4.2		0.84	16.8	
Total IWV uncertainty (2)[h]					0.81	2.0		0.76	3.5		0.69	13.8	

[a] The claimed 1-σ uncertainty of the IGS ZTD product.
[b] Taken from *Wang et al.* (2007) based on the comparison between NCEP/NCAR reanalysis and ground measurement.
[c] Taken from *Heise et al.* (2009) based on the comparison between ECMWF reanalysis and ground measurement.
[d] Taken from *Wang et al.* (2005) based on the comparison between NCEP/NCAR reanalysis and radiosonde data.
[e] Taken from *Wang et al.* (2005) based on the comparison between ECMWF reanalysis and radiosonde data.
[f] Taken from Table 1 in *Bevis et al.* (1994).
[g] Calculated using 1.7 hPa and 1.3 K for the uncertainties of P_0 and T_m, respectively.
[h] Calculated using 0.9 hPa and 1.1 K for the uncertainties of P_0 and T_m, respectively.
[i] Percentage of the total IWV uncertainty (1).
[j] The constant given in Equation (2.14).

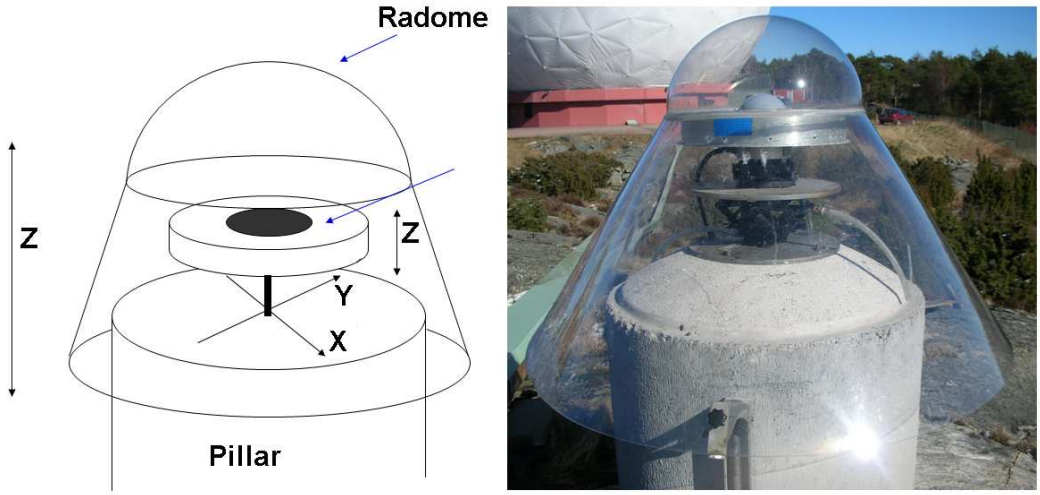

Figure 3.5: Schematic drawing and photograph of the experiment station (ONTE).

geometries of the microwave absorber and the radome, i.e. with or without radome, and with or without the absorber below or around the antenna. The experimental station was first used to investigate the effects on the estimated coordinates due to the geometry of the installation of the antenna and the equipment with the radome. The results show that the effects due to a change of the eccentric position of the antenna are not significant. The use of a properly placed radome does not affect the estimated results. Neither does a small (a few cm) misalignment of the radome. However, a large vertical change in the position of the radome (e.g. the radome raised by 10 cm) causes significant errors in the vertical coordinate (centimetres), which are possibly caused by the fact that GPS signals propagate through the interface of the hemispheric top and the conical base of the radome.

Paper B first demonstrates the positive impact of using the absolute antenna PCV calibration when analyzing GPS data. Thereafter, the effects from the implementation of microwave absorbing material below the antenna plane and around the sides of the antenna, and a properly centred radome on the estimates of the relative site coordinates and the atmospheric water vapour, are investigated. The results show that the use of the absorber decreases the change in the vertical component of the baseline from ∼27 mm to ∼4 mm when the elevation cutoff angle varies from 5° to 20°. The horizontal components are much less affected. The corresponding offset in the estimates of the IWV decreases from ∼1.6 kg/m^2 to ∼0.3 kg/m^2. Two different configurations of the absorber on the antenna give similar results. Small offsets are seen, less than 5 mm and 0.4 kg/m^2, in the estimates of the vertical component of the baseline and the IWV, respectively, for all five elevation cutoff angle solutions when the antenna is covered by a hemispherical radome.

Chapter 4

GPS Meteorology for Climate Applications

4.1 Detection of climate changes using GPS data

As discussed in Section 1.1.3, the long-term measurement of the IWV is of great importance due to its role as an independent data source to assess possible global warming scenarios.

Traditionally, radiosondes have been used to observe long time series of the IWV (*Gaffen et al.*, 1992; *Ross and Elliot* (1996, 2001)). The limitation of radiosonde data for climate research is that the derived IWV is not homogeneous over long time periods due to calibration uncertainties and sensor changes.

A WVR can also be used to provide IWV estimates (*Elgered and Jarlemark*, 1998). However, the WVR has not been proven to be sufficiently stable in terms of determining the long time series of the IWV. Furthermore, the WVR is not a commonly used instrument and it is inaccurate when the drop size is not significantly smaller than the observed wavelength, i.e. during rain.

The poor temporal and spatial resolutions of the VLBI-derived IWV limit the role of the VLBI technique for climate applications, except as an external data source for validation at selection locations, where it can be extremely useful.

Working under in principle all weather conditions with increasing spatial resolution locally and globally, the GPS technique seems to be superior to provide stable long time series of the IWV compared to the other techniques mentioned above.

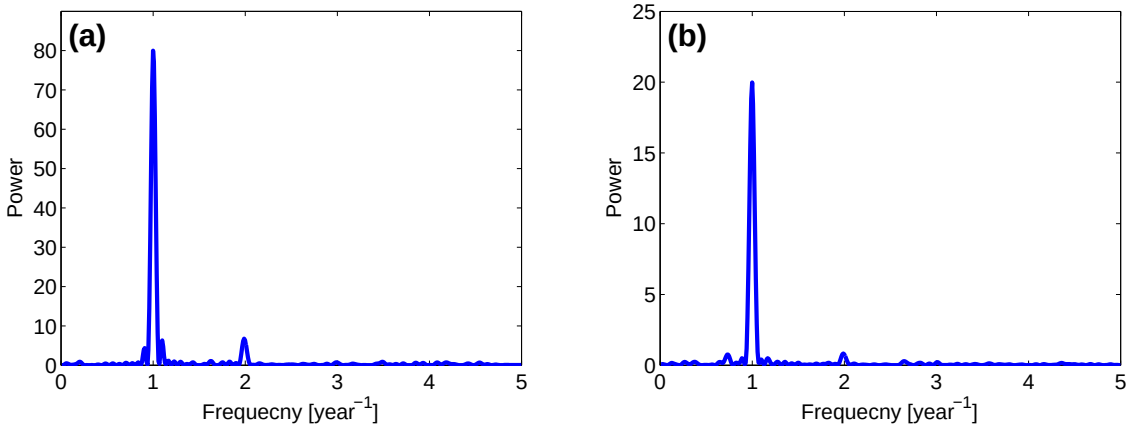

Figure 4.1: Lomb-Scargle periodograms for the IWV time series for (a) REYK and (b) BRAZ for the time period from January 1997 to December 2011.

4.1.1 Estimation of long-term trends in IWV

Linear trends of the IWV time series can be obtained using a model, which considers the seasonal variations in the IWV. For a GPS data set, the components needed to describe the seasonal variations can be investigated using the method of Lomb-Scargle periodograms (*Hocke*, 1998). Two examples are shown in Figure 4.1 for two GPS sites: REYK (−18.96 °E, 64.14 °N) and BRAZ (−47.88 °E, −15.95 °N). The results indicate that the most marked IWV variations are at the frequencies centring on the annual and the semi-annual terms. The diurnal and the semi-diurnal variations are observed in the high frequency range (not shown), which however have much smaller amplitudes causing insignificant impact on the resulting trend. Therefore, it is sufficient to use an annual and a semi-annual term to describe the seasonal variations in the IWV. The model used for the trend estimations is expressed as:

$$y = y_0 + a_1 t + a_2 \sin(2\pi t) + a_3 \cos(2\pi t) + a_4 \sin(4\pi t) + a_5 \cos(4\pi t) \quad (4.1)$$

where y is the IWV and t is the time in years. The parameters y_0 and a_1 are the mean offset and the linear trend of the IWV, respectively; a_2 and a_3 are the annual component coefficients, and a_4 and a_5 are the semi-annual component coefficients. All unknown coefficients are determined through the method of least squares.

Using Equation (4.1), IWV trends for 42 globally distributed GPS sites were estimated using 15 years of data (1 January 1997 to 31 December 2011) from the NCAR global, 2-hourly ground-based GPS IWV data set (*Wang et al.*, 2007). Two examples of the IWV time series together with the fitted seasonal components and the linear trends are shown in Figure 4.2 for REYK and BRAZ. It is evident that the model fits the seasonal pattern of the IWV well, while there are short-term variations with a time scale of a few weeks or less which are not described by the model.

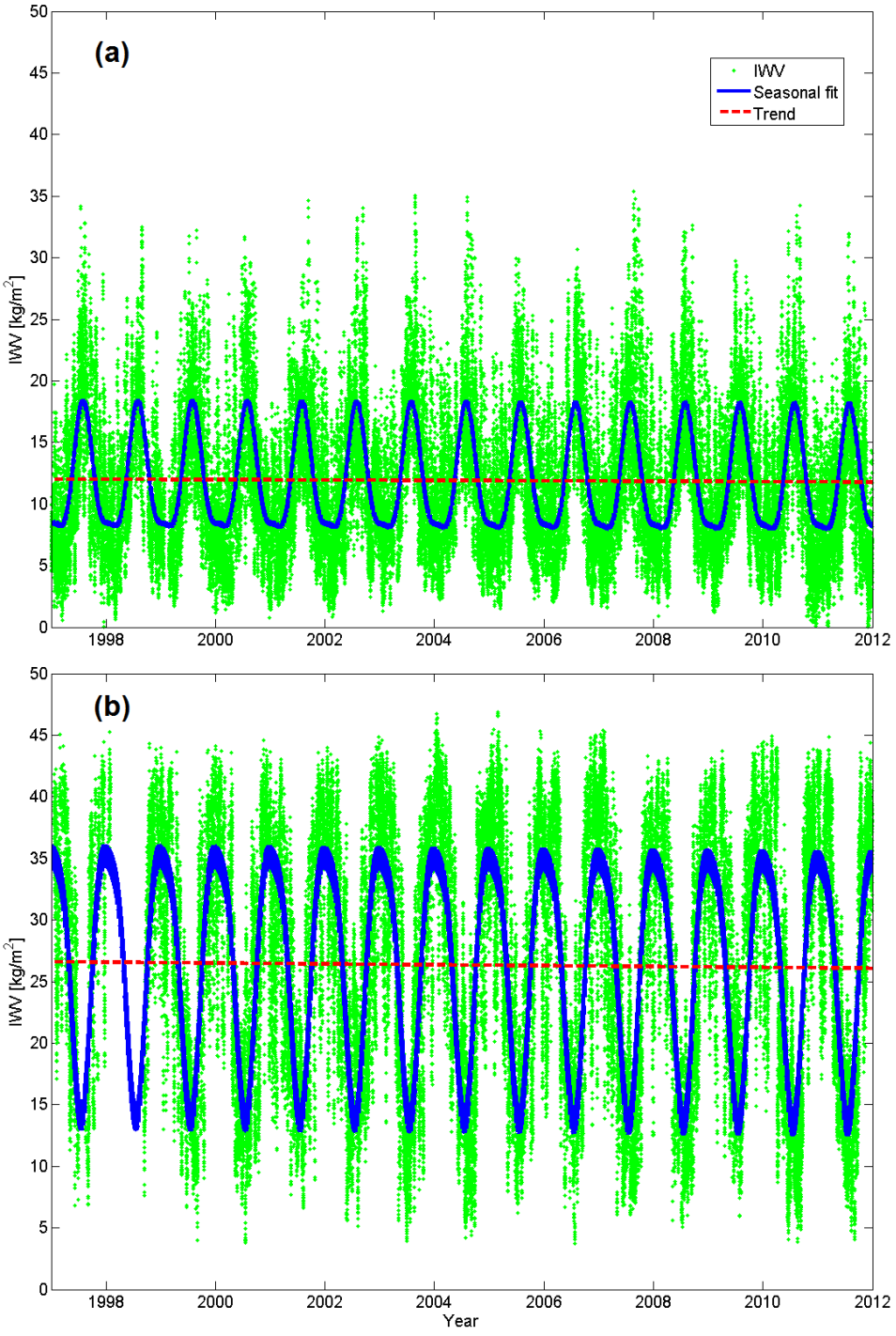

Figure 4.2: Examples of the time series of the IWV for (a) REYK and (b) BRAZ for the time period from January 1997 to December 2011. Displayed are also the fitted linear trends and the seasonal components.

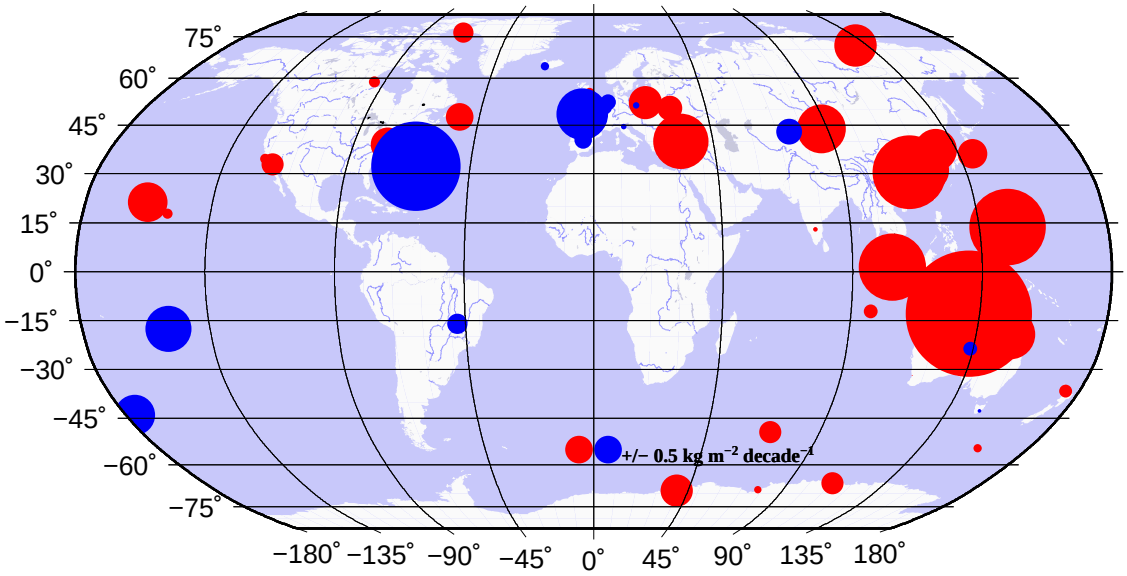

Figure 4.3: Linear IWV trends estimated for 42 global GPS sites for the time period from 1 January 1997 to 31 December 2011. The red circles mean positive trends and the blue circles mean negative trends.

Figure 4.3 depicts the geographical pattern of the obtained linear IWV trends, which are also given numerically in Table 4.1, for all sites. The trends are in the range from -1.65 kg/(m^2·decade) to $+2.32$ kg/(m^2·decade). In order to interpret these trends properly, the uncertainty of the trend needs to be discussed.

4.1.2 Uncertainty of the estimated IWV trend

The uncertainty of a linear trend is determined by many factors, i.e. the time span of available data, the magnitude of variability and the autocorrelation of the noise (*Weatherhead et al.*, 1998). Correspondingly, the uncertainty of our estimated IWV trend is determined by the length of IWV time series, the magnitude of the uncertainty of individual GPS-derived IWV, and the short-term variations in the IWV, which are not described by the model in Equation (4.1). *Weatherhead et al.* (1998) also pointed out that the detection of the true trend can be difficult when sudden changes occur in the data, such as when an instrument is changed. This could also happen to our GPS data set, e.g. due to antenna or radome changes, or an implementation of microwave absorbing material. Impacts from the above factors on the resulting IWV trend will be discussed in this section.

Uncertainty due to the short-term variation in IWV

In order to see how well the model (Equation (4.1)) fits the IWV time series, we used the chi-square statistic to investigate the residuals after the model fit. The quantity

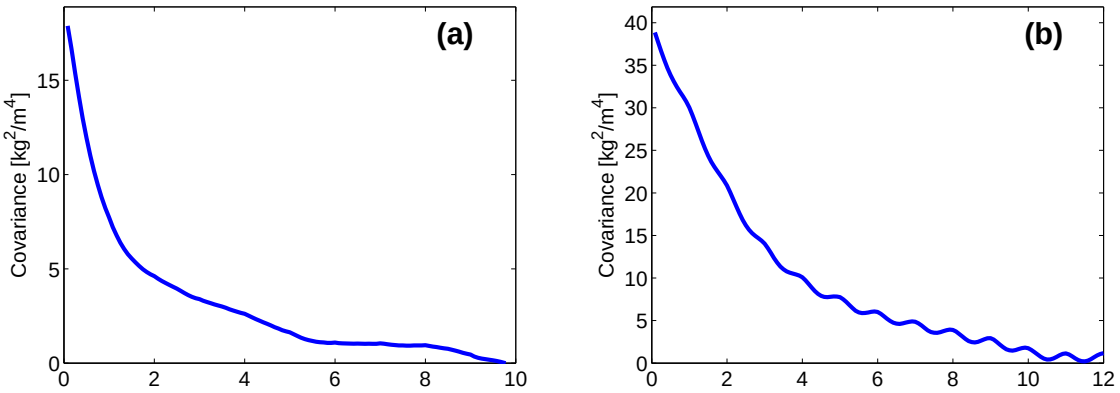

Figure 4.4: Covariance of the residuals after the model fit for two GPS sites: (a) REYK and (b) BRAZ.

is given as:

$$\chi^2 = \sum_{i=1}^{N} \frac{[V_i - \widehat{V}_i]^2}{\sigma_i^2} \tag{4.2}$$

where N is the number of data points; V_i and σ_i are the GPS-derived IWV and the corresponding uncertainty, respectively; and $\widehat{V}_i$ is the model fit.

If the model fits the IWV time series adequately, the variance of the residuals (s^2) should agree well with the uncertainty of the GPS-derived IWV (σ^2) and the ratio of s^2/σ^2 should be around 1. The ratio can be estimated by the reduced chi-square error (χ^2/v), where v is the number of degrees of freedom, usually given by N-n-1, and n is the number of unknown coefficients in Equation (4.1). Table 4.1 summarizes the reduced chi-square errors calculated for all 42 sites. For simplification, a common value of 0.76 kg/m^2, taken from Table 3.4, for the total IWV uncertainty (σ) was used in Equation (4.2) for all IWV estimates and for all sites. As shown in Table 4.1, all reduced chi-square values significantly deviate from 1, varying from 4 to 196, and tend to increase with decreasing absolute latitude. This implies that the residuals after the model fit are actually not white noise, due to the fact that the true short-term variability in the IWV is not modelled by Equation (4.1), and therefore residuals are correlated over several days. Two examples of such correlations are shown in Figure 4.4, where covariances calculated from the residuals after the model fit are demonstrated for REYK and BRAZ. A longer decorrelation time is seen for the BRAZ site, which is located at a lower latitude. In order to calculate the trend uncertainty after taking these short-term variations into account, a model which can describe the covariance between IWV values V_1 and V_2 observed at the time epochs t_1 and t_1 was used (*Nilsson and Elgered*, 2008):

$$Cov[\,V_1(t_1), V_2(t_2)\,] = a_1\, 2^{-|t_1-t_2|/T_1} + a_2\, 2^{-|t_1-t_2|/T_2} \tag{4.3}$$

Table 4.1: Reduced chi-square errors, estimated IWV trends, and corresponding uncertainties, for all 42 GPS sites, sorted by decreasing absolute latitude

GPS Site	Longitude [°E]	Latitude [°N]	χ^2/v	Trend [kg/(m^2·decade)]	Uncertainty[a] [kg/(m^2·decade)]
THU2	−68.83	76.54	8	0.38	0.24
TIXI	128.87	71.63	18	0.78	0.29
SYOG	39.58	−69.01	4	0.59	0.21
DAV1	77.97	−68.58	4	0.13	0.21
CAS1	110.52	−66.28	8	0.41	0.22
REYK	−21.96	64.14	33	−0.16	0.31
CHUR	−94.09	58.76	36	0.21	0.32
MORP	−1.69	55.21	44	0.18	0.33
MAC1	158.94	−54.50	36	0.16	0.26
JOZE	21.03	52.10	51	0.61	0.40
WROC	17.06	51.11	48	−0.12	0.36
BRUS	4.36	50.80	52	−0.29	0.37
GLSV	30.50	50.36	46	0.46	0.44
KERG	70.26	−49.35	49	0.41	0.29
BRST	−4.50	48.38	56	−0.95	0.41
STJO	−52.68	47.60	99	0.51	0.49
MEDI	11.65	44.52	52	−0.11	0.40
CHAT	−176.57	−43.96	63	−0.74	0.43
URUM	87.60	43.81	32	0.90	0.35
CHUM	74.75	43.00	37	−0.47	0.54
HOB2	147.44	−42.80	47	−0.06	0.28
VILL	−3.95	40.44	43	−0.32	0.37
USNO	−77.07	38.92	148	0.63	0.55
SUWN	127.05	37.28	112	0.78	0.51
AUCK	174.83	−36.60	81	0.23	0.43
TSKB	140.09	36.11	121	0.54	0.54
NICO	33.40	35.14	43	0.40	0.43
VNDP	−120.62	34.56	62	0.19	0.47
SIO3	−117.25	32.86	74	0.41	0.55
BRMU	−64.70	32.37	118	−1.65	0.48
SHAO	121.20	31.10	196	0.78	0.98
ALIC	133.89	−23.67	143	−0.25	0.90
HNLC	−157.86	21.30	72	0.73	0.71
HILO	−155.05	19.72	74	0.19	0.84
TOW2	147.06	−19.27	161	0.91	1.42
THTI	−149.61	−17.58	96	−0.85	0.73
BRAZ	−47.88	-15.95	71	−0.37	0.64
GUAM	144.87	13.59	104	1.41	0.65
IISC	77.57	13.02	88	0.08	0.72
DARW	131.13	−12.84	134	2.32	1.52
COCO	96.83	−12.19	154	0.25	1.23
NTUS	103.68	1.35	42	1.23	0.46

[a]The 1-σ formal uncertainty of the IWV trend after taking the short-term variations into account.

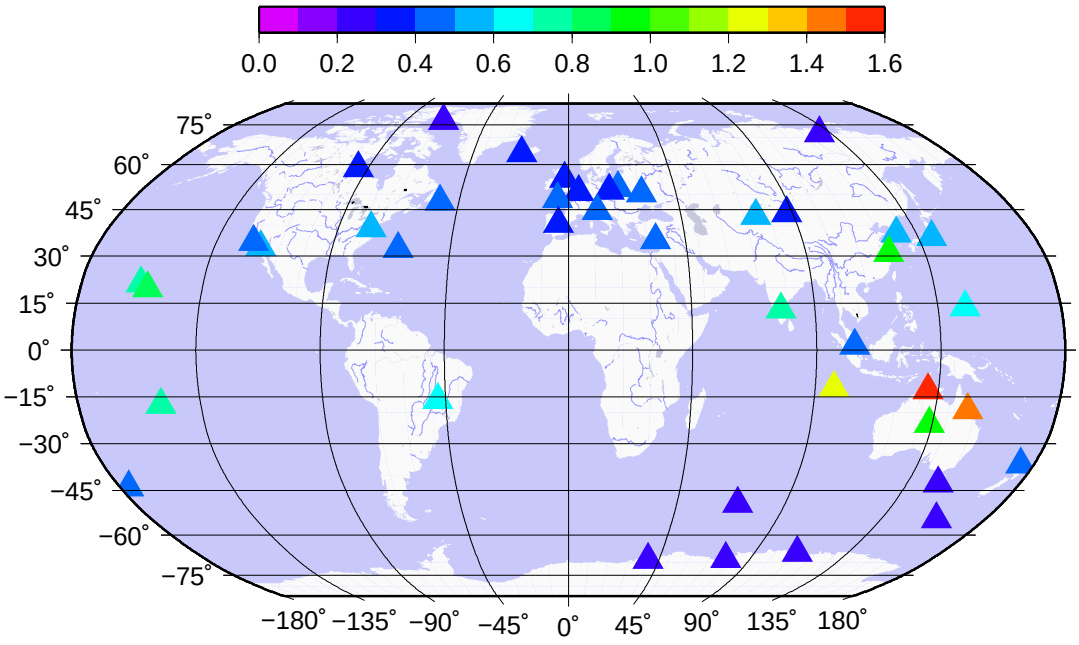

Figure 4.5: Uncertainties of the IWV trends for all 42 GPS sites after taking short-term variations into account.

In order to obtain the coefficients a_1, a_2, T_1, and T_2, the covariance of the residuals after the fit of the IWV to the model was first calculated. These were then used in a nonlinear least squares fit to obtain all the coefficients in Equation (4.3). From the covariance model, the covariance matrix (C) can be used for computing the trend uncertainty:

$$C_{error} = (X^T X)^{-1} X^T C X (X^T X)^{-1} \tag{4.4}$$

where X is the design matrix of Equation (4.1), and C_{error} is the covariance matrix for the uncertainties of the estimated parameters. The resulting trend uncertainties for all 42 GPS sites are shown in Figure 4.5 and summarized in Table 4.1. The uncertainties vary in the interval 0.21–1.52 kg/(m^2·decade), and large values are observed at latitudes between approximately −30 °N and +30 °N. Figure 4.6 depicts the ratio of the estimated IWV trends and corresponding trend uncertainties. It is evident that most of trends are insignificant given the magnitude of the uncertainty.

Uncertainty due to errors in the IWV estimate

The impact of the uncertainty in the individual IWV estimate (σ_{IWV}) on the resulting IWV trend can be approximated using the error covariance matrix expressed as:

$$C_{error} = (X^T X)^{-1} X^T \sigma^2_{IWV} X (X^T X)^{-1} \tag{4.5}$$

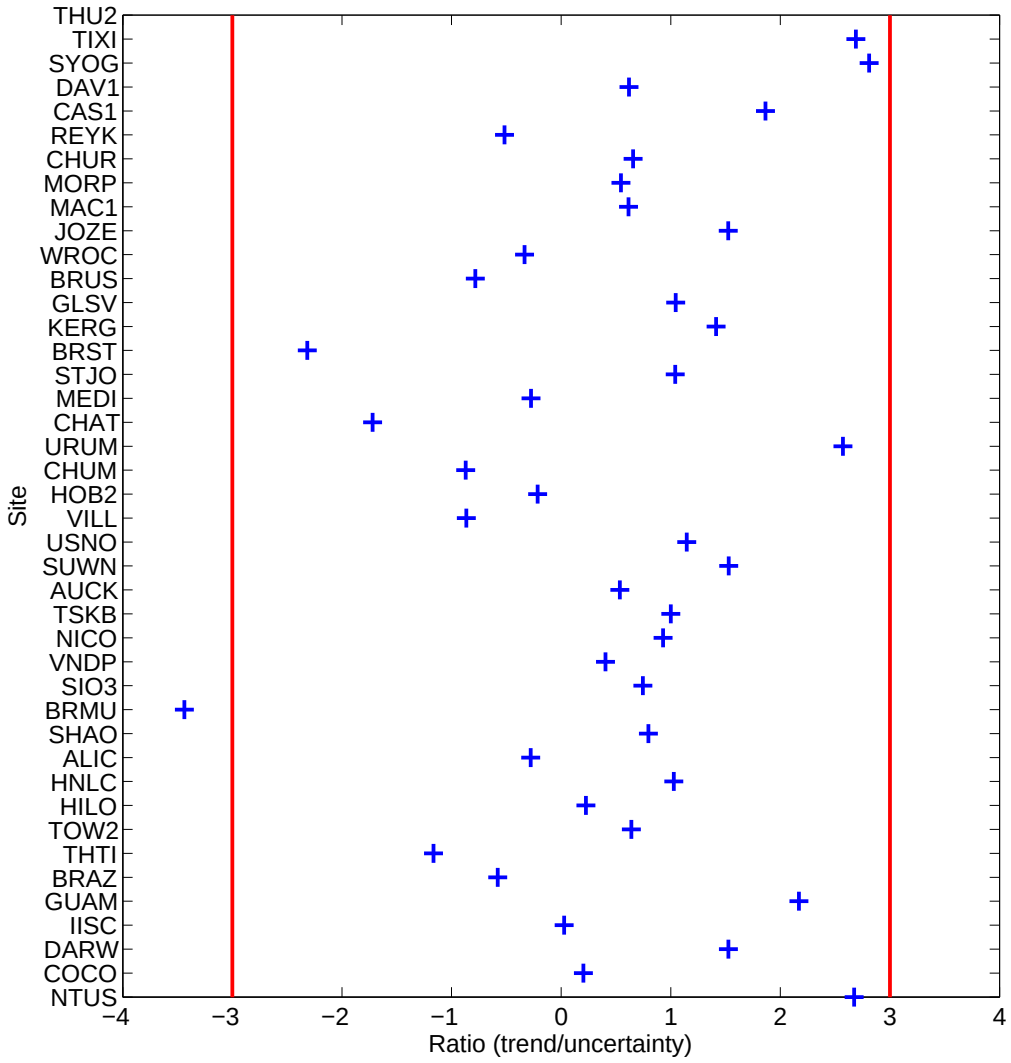

Figure 4.6: The ratio of the estimated IWV trends and corresponding trend uncertainties. Two solid red lines show the ± 3-σ.

Equation (4.5) is same as Equation (4.4), except assuming that the residuals after the model fit are described by white noise. If we still set the common value of σ_{IWV} as 0.76 kg/m^2, the resulting trend uncertainties for all 42 sites are less than 0.01 kg/(m^2·decade), which is much smaller than the trend uncertainties after taking the short-term variations of the IWV into account.

A complication in the IWV trend estimation is that changes during the operation of a GPS site may cause systematic effects in the IWV time series which may

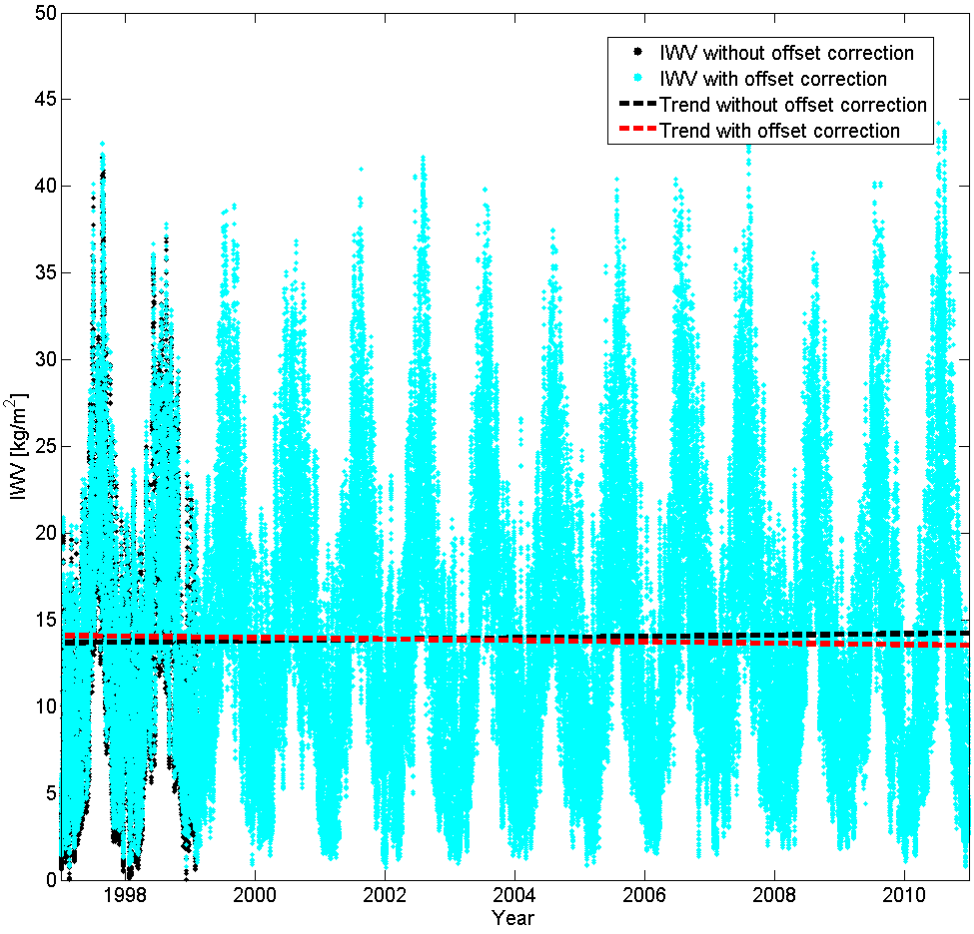

Figure 4.7: The IWV time series and linear trends for the ONSA site with and without applying an offset correction for the time period before the change of the radome (1 February 1999). The GPS-derived IWV were obtained using an elevation cutoff angle of 10°.

change the resulting trend. For example, the GPS site ONSA at the Onsala Space Observatory had a radome change on 1 February 1999, which may introduce an offset in the IWV time series. The magnitude of the offset can be determined from the IWV comparison between the GPS data and the one acquired from a co-located technique which is homogeneous. For the ONSA site, this was done by comparing the GPS-derived IWV to the IWV estimated from the VLBI data, which were acquired 78 m away from the GPS site. The IWV trends for ONSA estimated with and without applying an offset correction for the time period before the change of the radome are shown in Figure 4.7, where the corresponding trend changes from -0.2 kg/(m^2·decade) to $+0.2$ kg/(m^2·decade).

Signal multipath can also cause systematic errors in the GPS-derived IWV. Mul-

tipath effects are not fixed in time since they are sensitive to the surrounding environment which reflective properties may change, e.g. growing vegetation (*Granström and Johansson*, 2005) and/or different soil moisture (*Larson et al.*, 2010). The multipath impact is larger for observations at low elevation angles, which are included in order to improve the geometry and reduce the formal error of the individual IWV estimate. Therefore, higher elevation cutoff angles are desired for the IWV trend estimation due to the fact that the formal error of the IWV has much smaller impact on the resulting trend (see Paper C).

In summary, due to the relative short time period of the GPS-derived IWV (15 years), the short-term variations in the IWV dominate the uncertainty of the estimated linear trends. It should also be pointed out that the impact from the systematic error due to the specific change related to an instrument cannot be ignored. The correction for such errors is necessary.

4.2 Summary of Paper C

In GPS data sets, errors caused by atmospheric mapping functions (*Stoew et al.*, 2007), antenna PCV (*Schmid et al.*, 2007), and signal multipath (*Elósegui et al.*, 1995) all depend on the elevation angle. The systematic errors due to the first two factors can be significantly reduced by using new mapping functions and including a model for the correction of the antenna PCV (*Fang et al.*, 1998). For estimating the long-term trend of the IWV, systematic errors due to signal multipath would be insignificant if they were constant over the whole time series. However, this is not always true since the signal multipath is also sensitive to the surrounding environment (*Granström and Johansson*, 2005; and *Larson et al.*, 2010). The multipath effects are larger for observations at low elevation angles. Therefore, higher elevation cutoff angles may be desired for the IWV trend estimation due to the fact that the formal error of the IWV is not the limiting factor for this application (*Nilsson and Elgered*, 2008).

In Paper C, 14 years of data from 12 GPS sites in Sweden and Finland were used to estimate the IWV trends for 8 different elevation cutoff angles, from 5° to 40°, for the observations used in the analyses. The resulting GPS-derived IWV trends were compared to the corresponding trends obtained from radiosonde data at 7 nearby (< 120 km) sites. The highest correlation coefficient of 0.88 is obtained for the 25° solution, whereas the smallest RMS differences between the IWV estimates themselves are obtained mainly for elevation cutoff angles of 10° and 15°. The results show that elevation-angle-dependent systematic errors vary with time. Therefore, the elevation cutoff angle giving the best agreement between radiosonde and GPS for individual IWV estimates is not necessarily the optimum when estimating linear trends.

4.3 Evaluation of climate models using GPS data

The Earth's climate system involves a variety of processes operating on different temporal and spatial scales. Global simulations of the most of these processes are given by Global Climate Models (GCMs) which are able to simulate the climate system including its changes over time. The simulations for the past and the present are of great importance for us to understand the Earth's climate system and causes for climate change. GCMs are also used to simulate the response of the climate system to current and future changes in radiative forcing (*Meehl et al.*, 2007), e.g. the increase of the greenhouse gas. These responses are normally referred to as climate feedbacks.

Based on the comparison of the global climate feedback processes for several GCMs, *Bony et al.* (2006) found out that the water vapour feedback is the most important climate feedback. In addition, as discussed before, the movement of water vapour through the hydrological cycle is strongly coupled to precipitation and soil moisture, and redistributes energy. The vital role of water vapour in the climate system requires that climate models can represent these atmospheric processes for different spatial resolutions (from scales of micrometres up a few thousands of kilometres). However, typically a GCM operates on a spatial resolution of 100–300 km.

In order to obtain a finer spatial resolution, the local climate is often simulated using Regional Climate Models (RCMs) which operate on a horizontal resolution, typically from 10 km to 50 km (*Rummukainen*, 2010). Running with appropriate boundary conditions RCMs have been shown to reproduce many important features of the regional/local climate (*Christensen et al.*, 2010). Over the western Arctic Ocean, *Wyser et al.* (2008) evaluated eight RCMs using the same boundary conditions. They found that vertically integrated water vapour are reasonably well simulated at monthly and daily timescales, but with considerable differences between individual models.

The regional Rossby Centre Atmospheric (RCA) climate model is developed at the Swedish Meteorological and Hydrological Institute (SMHI) in order to provide regional climate scenarios. The RCA model versions have been run using the European Centre for Medium-Range Weather Forecasts (ECMWF) reanalysis data as boundary conditions. The IWV from the RCA simulation will differ from the ECMWF reanalysis due to the the data assimilation done in ECMWF, which keeps the model closer to the observations. Meanwhile, the stability of the IWV time series from the ECMWF data is limited due to changes in the observing systems (*Bengtsson et al.*, 2004). Therefore, evaluation of the IWV simulated by climate models using independent observations of the IWV with a high accuracy is necessary.

Given the ability of operating under almost all weather conditions and the long-

term stability, the GPS technique has a superiority to measure long time series of the IWV with a temporal resolution as high as a few minutes (*Wang and Zhang*, 2009). As GPS receivers are increasing in numbers globally and locally, the spatial resolution of the GPS-derived IWV will also be improved. Meanwhile, as discussed in Section 3.2, the uncertainty of the GPS-derived IWV is possible to be below 1 kg/m^2. In addition, different to the radiosonde data, the GPS data have not yet been assimilated in any climate reanalysis products, which makes them an independent data set suitable for the evaluation of climate models.

The IWV time series inferred from the ground-based GPS measurements can be used to assess climate models in term of the following aspects:

- Evaluation of the representation of the IWV in the models by comparing the model simulation to the GPS-derived IWV. Using the IWV obtained from GPS networks can identify model deficiencies for different weather systems, land, and coastal areas.

- The diurnal cycle is one of the most obvious and reliable signals of the climate. Therefore, given its high temporal resolution, GPS-derived IWV is desired to evaluate the ability of climate models to simulate the diurnal cycles of the IWV. One example is shown in Figure 4.8 where the diurnal cycles for 14 consecutive summer months (from 1997 to 2010): June, July, and August, were estimated at 42 GPS sites using the GPS-derived IWV and the simulation from the RCA model. A detailed discussion about the IWV obtained from the GPS data and the RCA simulation is given in Paper D. The result shows a good agreement between the GPS and the model data in term of diurnal phases. The amplitude for the GPS data varies from 0.05 kg/m^2 to 1.48 kg/m^2 while a smaller amplitude (from 0.07 kg/m^2 to 0.62 kg/m^2) is seen for the diurnal cycle given by the model. This is consistent to the result presented by *Pramualsakdikul et al.* (2007) where the IWV diurnal cycles estimated using the GPS data (1998-2004) at 14 equatorial sites were compared to corresponding estimates by two numerical weather models. Figure 4.8 also depicts an evident increase of the amplitude along with the increase of the site latitude for the GPS data, which however is not clear for the model simulation.

- Comparison of the GPS-derived IWV to the model simulation applying different horizontal resolution can be used to investigate the sensitivity of the model grid point chosen for the IWV representation. The vertical transport of water vapour is sensitive to the model vertical resolution. Therefore, comparisons to the model simulation run with different verticals resolution can also provide useful information.

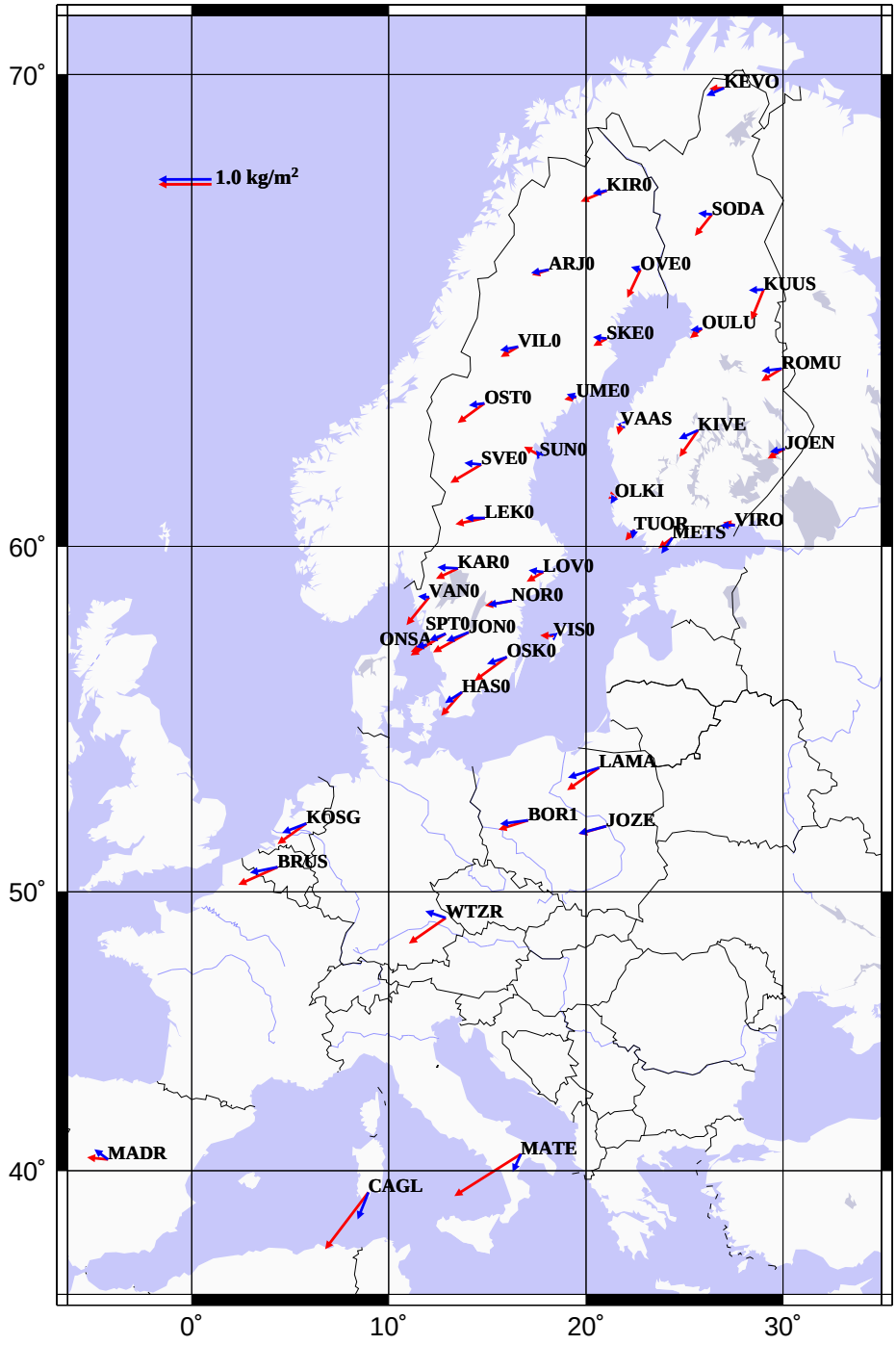

Figure 4.8: Estimated amplitude and phase of the IWV diurnal cycle for 14 years consecutive summers from the GPS data (red arrows) and from the simulation of the RCA model (blue arrows). The phase is illustrated by the vector direction in a clock-wise sense where up corresponds to midnight and down corresponds to noon.

4.4 Summary of Paper D

This paper focuses on the use of ground-based GPS measurements for the evaluation of the RCA climate model. We used GPS measurements with a maximum length of 14 years (1 January 1997 to 31 December 2010) acquired at 99 European sites in order to estimate IWV for the assessment. The RCA simulation was driven at the boundaries by ECMWF reanalysis data (ERA Interim). The RCA horizontal resolution was 50 km and 24 vertical levels and the IWV value was stored every half-hour. The IWV obtained from the ERA Interim reanalysis were also used for comparisons and were interpolated to the RCA grid. Model data were obtained from the nearest gridpoint to each GPS site after the vertical interpolation to the GPS height.

The comparisons (model−GPS) show that monthly mean IWV differences of 0.47 kg/m^2 and 0.39 kg/m^2 are obtained for the RCA simulation and for the ECMWF data, respectively. A larger standard deviation of the IWV difference (0.98 kg/m^2) is seen for the RCA−GPS comparison while the one for ECMWF−GPS is 0.35 kg/m^2. The IWV difference for the RCA model is positively correlated to the difference for the ECMWF model. However, this is not the case for two sites in Italy where a wet bias is seen for ECMWF while a dry bias is seen for RCA. The RCA−GPS comparison shows a significant seasonal variation. RCA is too dry in the summer. Models tend to give a larger IWV (more significant for the RCA model) for the sites nearby sea where the surface tile of the model gridpoint has a water coverage larger than 60 %. This is, however, expected since the IWV value obtained from models is the mean for the gridbox depending on the surface type, i.e. water, open land, forest, and snow. Since the evaporation is larger from a water surface, it will dominate the mean value and can affect the IWV differences for such points when comparing to a land based GPS data.

Chapter 5

Conclusions

The vital role of water vapour in the Earth's climate system requires the measurements of the atmospheric Integrated Water Vapour (IWV) with a long-term stability and a high accuracy. This work presented different procedures, and methods which are used by some of the techniques in order to infer IWV, with a main focus on the Global Positioning System (GPS).

The advantages of the GPS measurements are that they can be performed independently on the weather and have a high temporal resolution (a few minutes) on the IWV estimates. Meanwhile, along with densification and extension of permanent GPS site networks globally and regionally, a continuously improving spatial resolution is expected. Therefore, using the GPS measurements to provide estimates of the IWV above receivers on the ground is a promising application.

In order to assess the quality of the IWV estimates, two methods were presented to calculate the final uncertainty of the GPS-derived IWV. A statistical analysis was first presented using the results from the comparisons of a 10-year-long time series of the atmospheric Zenith Wet Delay (ZWD) estimated using the Global Positioning System (GPS), geodetic Very Long Baseline Interferometry (VLBI), a Water Vapour Radiometer (WVR) which are co-located at the Onsala Space Observatory (see Paper A). The calculated uncertainty of the GPS-derived IWV varies from $\sim$0.5 kg/m^2 to $\sim$1 kg/m^2 depending on the offset used in the VLBI-derived ZWD. Using a theoretical analysis, the final uncertainty of the IWV can be calculated using the uncertainties associated with different variables involved in the procedure where the equivalent Zenith Total Delay (ZTD) estimated from the GPS data is converted to the IWV. The result shows that it is the ZTD uncertainty that dominates over other errors. The accuracy of the ZTD estimates depends on many parameters, i.e. satellite orbit errors, ionospheric delay, signal multipath, antenna related errors (e.g. phase centre variations), and mapping functions. The claimed 1-σ uncertainty (4 mm) given by the International GNSS Service (IGS) ZTD product is a good assumption for a low threshold and is supported by the results presented

by our statistical analysis for the Onsala GPS site. Using the 4 mm ZTD uncertainty and the uncertainties for other variables presented by many previous studies, we found that globally an uncertainty of less than 1 kg/m^2 is achievable for the GPS-derived IWV.

The long-term measurement of the IWV is of great importance due to its role as an independent data source to detect climate changes. Given its long-term stability and high accuracy, the GPS-derived IWV is desired for the climate applications in terms of the estimation of linear IWV trends. Using 15 years of data (1 January 1997 to 31 December 2011) from the National Center for Atmospheric Research (NCAR) global, 2-hourly ground-based GPS IWV data set, the estimated IWV trends are in a range from -1.65 kg/(m^2·decade) to $+2.32$ kg/(m^2·decade). These values, however, are comparable to the trend uncertainties, varying from 0.21 kg/(m^2·decade) to 1.52 kg/(m^2·decade). The major part of the trend uncertainty is caused by the true short-term variations of the IWV which cannot be modelled accurately. The rest of part is due to the uncertainty in the individual IWV estimate caused by random and systematic errors, where the latter one (if not fixed over time) has a larger impact on the trend estimation and is normally elevation dependent (see Paper B). The results from Paper C show that for the time period investigated and for the region of Fennoscandia, an elevation cutoff angle of 25° used in the GPS data analysis is optimum for the trend estimation, which gives the highest correlation (0.88) to the corresponding trends obtained from radiosonde data at nearby sites. However, the smallest root-mean-square differences between the IWV estimates themselves are obtained mainly for elevation cutoff angles of 10° and 15°. The results show that elevation-angle-dependent systematic errors vary with time. Therefore, the elevation cutoff angle giving the best agreement between radiosonde and GPS for individual IWV estimates is not necessarily the optimum when estimating linear trends. In addition, the correlation between the trends from the two completely independent techniques is also strong evidence that the two techniques provide information on the IWV trends although the true individual values are too small to be uniquely detected.

As an independent data set and given that its uncertainty does not depend on the absolute value of the IWV (see Paper A), the GPS-derived IWV is desired for the evaluation of climate models. In Paper D, the IWV derived from the GPS measurements with a maximum time period from January 1997 to December 2010 at 99 European sites were compared to the IWV simulated by the regional Rossby Centre Atmospheric (RCA) climate model, which was driven at the boundaries by the European Centre for Medium-Range Weather Forecasts (ECMWF) reanalysis data (ERA Interim). The focus of the comparison is on the monthly mean difference. Overall, an IWV difference of about 0.5 kg/m^2 was obtained by the RCA$-$GPS comparison. A significant seasonal variation is seen in the IWV difference (RCA is too dry in the summer). Meanwhile, the RCA model tends to underestimate

IWV for two sites in Italy. This is in accordance with a cold temperature bias and underestimate of temperature diurnal range for the model which leads to less surface evaporation and hence an underestimate of IWV. In addition, the comparison for the sites, where the surface tile of the model gridpoint has more than 60 % water coverage, shows a larger IWV difference. This is, however, expected when comparing the gridded model data (given by a mean value) to the GPS data from a specific land based site. We also demonstrated the diurnal cycles of the IWV estimated using the GPS data and the RCA simulation. Overall a good agreement was obtained for the phase while a smaller amplitude is seen in the results from the model.

Bibliography

Bar-Sever, Y.E., P.M. Kroger, and J.A. Borjesson, Estimating horizontal gradients of tropospheric path delay with a single GPS receiver, *J. Geophys. Res.*, 103(B3), 5,019–5,035, doi:10.1029/97JB03534, 1998.

Bengtsson, L., S. Hagemann, and K.I. Hodges, Can climate trends be calculated from reanalysis data?, *J. Geophys. Res.*, 109, D11111, doi:10.1029/2004JD004536, 2004.

Bengtsson, L., The global atmospheric water cycle, *Environ. Res. Lett.*, 109, doi:10.1088/1748-9326/5/2/025002, 2010.

Bevis, M., S. Businger, T. Herring, C. Rocken, R. Anthes, and R. Wave, GPS meteorology: remote sensing of atmospheric water vapor using the global positioning system, *J. Geophys. Res.*, 97(D14), 15, 787–801, doi:10.1029/92JD01517, 1992.

Bevis, M., S. Chiswell, T.A. Herring, R.A. Anthes, C. Rocken, and R.H. Ware, GPS meteorology: Mapping zenith wet delays onto precipitable water, *J. Appl. Meteorol.*, 33, 379–386, 10.1175/1520-0450(1994)033<0379:GMMZWD>2.0.CO;2., 1994.

Blewitt, G., Advances in Global Positioning System technology for geodynamics investigations: 1978-1992, in D.Smith and D. Turcotte, editors, *Contributions of Space Geodesy to Geodynamics: Technology*, 25, 195–213, 1993.

Bobak, J.P., and C.S. Ruf, A new model for the structure function of integrated water vapor in turbulence, *Radio Sci.*, 34, 1,461–1,473, doi:10.1029/1999RS900097, 1999.

Boehm, J., B. Werl, and H. Schuh, Troposphere mapping functions for GPS and very long baseline interferometry from European Centre for Medium-Range Weather Forecasts operational analysis data, *J. Geophys. Res.*, 111, B02406, doi:10.1029/2005JB003629, 2006.

Bony, S., R. Colman, V.M. Kattsov, R.P. Allan, C.S. Bretherton, J.-L. Dufresne, A. Hall, S. Hallegatte, M.M. Holland, W. Ingram, D.A. Randall, B.J. Soden, G. Tselioudis, and M.J. Webb, How well do we understand and

evaluate climate change feedback processes?, *J. Clim.*, 19(15), 3,445–3,482, doi:http://dx.doi.org/10.1175/JCLI3819.1, 2006.

Buehler, S.A., A. von Engeln, E. Brocard, V.O. John, T. Kuhn, and P. Eriksson, Recent developments in the line-by-line modeling of outgoing longwave radiation, *J. Quant. Spectrosc. Radiat. Transfer*, 98, 12, 446–457, doi:10.1016/j.jqsrt.2005.11.001, 2006.

Byun, S., and Y. Bar-Sever, A new type of troposphere zenith path delay product of the international GNSS service, *J. Geod.*, 83(3), 367–373, doi:10.1007/s00190-008-0288-8, 2009.

Chaboureau, J.-P., A. Chédin, and N.A. Scott, Remote sensing of the vertical distribution of atmospheric water vapor from the TOVS observations: Method and validation, *J. Geophys. Res.*, 103(D8), 8,743–8,752, doi:10.1029/98JD00045, 1998.

Christensen, J., E. Kjellström, F. Giorgi, G. Lenderink, and M. Rummukainen, Weight assignment in regional climate models, *Climate Res.*, 44(2–3), 179–194, 2010.

Combrink, A., M.S. Bos, R.M. Fernandes, W.L. Combrinck, and C.L. Merry, On the importance of proper noise modelling for long-term precipitable water vapour trend estimations, *S. Afr. J. Geol.*, 110, 211–218, doi:10.2113/gssajg.110.2-3.211, 2007.

Davies, H.C., A lateral boundary formulation for multi-level prediction models. *Q. J. R. Meteorol. Soc.*, 102, 405–418, doi:10.1002/qj.49710243210, 1976.

Davis, J.L., T. Herring, I.I. Shapiro, A. Rogers, and G. Elgered, Geodesy by radio interferometry: Effects of atmospheric modeling errors on estimates of baseline length, *Radio Sci.*, 20, 1,593–1,607, doi:10.1029/RS020i006p01593, 1985.

Davis, J.L., G. Elgered, A.E. Niell, and C.E. Kuehn, Ground-based measurement of gradients in the "wet" radio refractivity of air, *Radio Sci.*, 28(6), 1,003–1,018, doi:10.1029/93RS01917, 1993.

Douša, J., The impact of errors in predicted GPS orbits on zenith troposphere delay estimation, *GPS solut.*, 14, 229–239, doi:10.1007/s10291-009-0138-z, 2010.

Elgered, G., Tropospheric radio path delay from ground-based microwave radiometry, *in Atmospheric Remote Sensing By Microwave Radiometry*, 215–258, Wiley & Sons, Inc, 1993.

Elgered, G., and P.O.J. Jarlemark, Ground-based microwave radiometry and long-term observations of atmospheric water vapor, *Radio Sci.*, 33, 707–717, doi:10.1029/98RS00488, 1998.

Elgered, G., B. Stoew, L. Gradinarsky, and H. Bouma, Analysis of atmospheric parameters derived from ground-based GPS observations, *In proceedings of he International Workshop on GPS Meteorology*, Tsukuba, Japan, edited by R.A.A. Anthes, 3–11, Japan Int. Sci. and Technol. Exchange Cent., 2003.

Elósegui, P., J.L. Davis, R.T.K. Jaldehag, J.M. Johansson, A.E. Niell, and I.I. Shapiro, Geodesy using the Global Positioning System: the effects of signal scattering on estimates of site position, *J. Geophys. Res.*, 100, B6, 9,921–9,934, doi:10.1029/95JB00868, 1995.

Emardson, T.R., J.M. Johansson, and G. Elgered, The systematic behavior of water vapor estimates using four years of GPS observations, *Trans. IEEE Geosci. Remote Sens.*, 38, 324–329, doi:10.1109/36.823927, 2000.

Fang, P., M. Bevis, Y. Bock, S. Gutman, and D. Wolfe, GPS meteorology: Reducing systematic errors in geodetic estimates for zenith delay, *Geophys. Res. Lett.*, 25, 19, 3,583–3,586, doi:10.1029/98GL02755, 1998.

Fritsche, M., R. Dietrich, C. Knöfel, A. Rülke, and S. Vey, Impact of higher-order ionospheric terms on GPS estimates, *Geophys. Res. Lett.*, 32, L23311, doi:10.1029/2005GL024342, 2005.

Gaffen, D.J., W.P. Elliott, and A. Robock, Relationship between tropospheric water vapor and surface temperatures as observed by radiosondes, *Geoph. Res. Lett.*, 19, 1,839–1,842, doi:10.1029/92GL02001, 1992.

Gradinarsky, L.P., J.M. Johansson, H.R. Bouma, H.-G. Scherneck, and G. Elgered, Climate monitoring using GPS, *Phys. Chem. Earth*, 27, 225–340, doi:10.1016/S1474-7065(02)00009-8, 2002.

Granström, C., and J.M. Johansson, The Influence of Vegetation and Multipath on GNSS signals, *in proc. Radio Science and Communication*, Linköping, Sweden, June 14-16, 385–390, 2005.

Greenhouse Gases and Greenhouse Effect, *World of Earth Science.*, Ed. K. Lee Lerner and Brenda Wilmoth Lerner, 1, Gale Cengage, http://www.enotes.com/greenhouse-gases-greenhouse-effect-reference, 2003.

Haas, R., G. Elgered, L. Gradinarsky, and J.M. Johansson, Assessing long term trends in the atmospheric water vapor content by combining data fromVLBI, GPS, radiosondes and microwave radiometry, *In: Schwegmann W, Thorandt V (eds) Proceedings of the 16th Working Meeting on European VLBI for Geodesy and Astrometry*, Bundesamt für Kartographie und Geodäsie, Leipzig/Frankfurt am Main, 279–288, 2003.

Hagemann, S., L. Bengtsson, and G. Gendt, On the determination of atmospheric water vapor from GPS measurements, *J. Geophys. Res.*, 108, D21, 4678, doi:10.1029/2002JD003235, 2003.

Heise, S., J. Wickert, G. Beyerle, T. Schmidt, and Ch. Reigber, Global monitoring of tropospheric water vapor with GPS radio occultation aboard CHAMP, *Adv. Space. Res.*, 37, 12, 2,222–2,227, http://dx.doi.org/10.1016/j.asr.2005.06.066 , 2006.

Heise, S., G. Dick, G. Gendt, T. Schmidt, and J. Wickert, Integrated water vapor from IGS ground-based GPS observations: initial results from a 5-min data set, *Ann. Geophys.*, 27, 2,851–2,859, 2009.

Hernández-Pajares, M., J.M. Juan, J. Sanz, and R. Oruz, Second-order ionospheric term in GPS: Implementation and impact on geodetic estimates, *J. Geophys. Res.*, 112, B08417, 1–16, doi:10.1029/2006JB004707, 2007.

Hill, E.M., J.L. Davis, P. Elósegui, B.P. Wernicke, E. Malikowski, and N.A. Niemi, Characterization of site-specific GPS errors using a short-baseline network of braced monuments at Yucca Mountain, southern Nevada, *J. Geophys. Res.*, 114, B11402, doi:10.1029/2008JB006027, 2009.

Hocke, K., Phase estimation with Lomb-Scargle periodogram method, *Ann. Geophys.*, 16, 356–358, 1998.

Immler, F.J., J. Dykema, T. Gardiner, D.N. Whiteman, P.W. Thorne, and H. Vömel, Reference Quality Upper-Air Measurements: guidance for developing GRUAN data products, *Atmos. Meas. Tech.*, 2, 1,217–1,231, doi:10.5194/amt-3-1217-2010, 2010.

Ingold, T., B. Schmid, C. Matzler, P. Demoulin, and N. Kampfer, Modeled and empirical approaches for retrieving columnar water vapor from solar transmittance measurements in the 0.72, 0.82 and 0.94m absorption bands, *J. Geophys. Res.*, 105(D19), 24,327–24,344, doi:10.1029/2000JD900392, 2000.

Intergovernmental Panel on Climate Change,Climate Change 2007: The Physical Science Basis-Contribution of Working Group I to the Fourth Assessment Report of the Intergovernmental Panel on Climate Change, *Cambridge Univ. Press*, Cambridge, U.K., 2007.

Jarlemark, P.O.J., Microwave radiometry for studies of variations of atmospheric water vapour and cloud liquid content, *Technicla report No. 181L*, Chalmers University of Technology, Gothenburg, Sweden, 1994.

Jarlemark, P.O.J., Analysis of temporal and spatial variations in atmospheric water vapor using microwave radiometry, *PhD Thesis, Technicla report No. 308*, Chalmers University of Technology, Gothenburg, Sweden, 1997.

Johansson, J.M., J.L. Davis, H.-G. Schernech, G.A. Milne, M. Vermeer, J.X. Mitrovica, R.A. Bennett, B. Jonsson, G. Elgered, P. Elósegui, H. Koivula, M. Poutanen, B.O. Rönnäng, and I.I. Shapiro, Continuous GPS measurements of postglacial adjustment in Fennoscandia, *J. Geophys. Res.*, 1079(B8), doi:10.1029/2001B000400107, 2002.

Jury, M.R., and D. Waliser, Satellite microwave measurements of atmospheric water vapour and marine wind speed: case study application, *S. Afr. J. mar. Sci.*, 9, 309-316, doi:10.2989/025776190784378943, 1990.

Klobuchar, J.A., Ionospheric Effects on Satellite Navigation and Air Traffic Control Systems, *AGARD Lect. Ser.*, 93, Advisory Group for Aerospace Res. and Dev., North Atlantic Treaty Org., Brussels, 1978.

Kondratev, K.Ya., Radiation processes in the atmosphere, *Geneva: World Meteorological Organization*, 1972.

Kuo, Y.-H., Y.-R. Guo, and E.R. Westwater, Assimilation of precipitable water measurements into a mesoscale numerical model, *Mon. Weather Rev.*, 121, 1,215-1,238, doi:10.1175/1520-0493(1993)121<1215%3AAOPWMI>2.0.CO;2, 1993.

Larson, K.M., J.J. Braun, E.E. Small, V.U. Zavorotny, E.D. Gutmann, and A.L. Bilich, GPS multipath and its relation to near-surface soil moisture content, *IEEE J-STARS*, 3, 1, 91–99, 10.1109/JSTARS.2009.2033612, 2010.

Mears, C., B.D. Santer, F.J. Wentz, K. Taylor, and M. Wehner, Relationship between temperature and precipitable water changes over tropical oceans, *Geophys. Res. Lett.*, 34, L24709, doi:10.1029/ 2007GL031936, 2007.

Meehl, G., T. Stocker, W. Collins, P. Friedlingstein, A. Gaye, J. Gregory, A. Kitoh, R. Knutti, J. Murphy, A. Noda, S. Raper, I. Watterson, A. Weaver, and Z.-C. Zhao, Global climate projections. In Climate Change 2007: The Physical Science Basis. Contribution of Working Group I to the Fourth Assessment Report of the Intergovernmental Panel on Climate Change, edited by S. Solomon, D. Qin, M. Manning, Z. Chen, M. Marquis, K. Averyt, M. Tignor, and H. Miller, *Cambridge University Press*, Cambridge, United Kingdom and New York, NY, USA, 2007.

Miloshevich, L.M., H. Vömel, D.N. Whiteman, and T. Leblanc, Accuracy assessment and correction of Vaisala RS92 radiosonde water vapor measurements, *J. Geophys. Res.*, 114, D11305, doi:10.1029/2008JD011565. 2009.

Niell, A., Global mapping functions for the atmosphere delay at radio wavelengths, *J. Geophys. Res.*, 101, 3,227–3,246, 1996.

Niell, A., Improved atmospheric mapping functions for VLBI and GPS, *Earth Planets Space*, 52, 699–702, doi:10.1029/95JB03048, 2000.

Nilsson, T., and G. Elgered, Long-term trends in the atmospheric water vapor content estimated from ground-based GPS data, *J. Geophys. Res.*, 113, D19101, doi:10. 1029/2008JD010110, 2008.

Owens, J.C., Optical refractive index of air: Dependence on pressure, temperature, and composition, *Appl. Opt.*, 6, 51–58, 1967.

Petrie, E.J., M.A. King, P. Moore, and D.A. Lavallée, Higher-order ionospheric effects on the GPS reference frame and velocities, *J. Geophys. Res.*, 115, B03471, doi:10.1029/2009JB006677, 2010.

Pireaux, S., P. Defraigne, L. Wauters, N. Bergeot, Q. Baire, and C. Bruyninx, Higher-order ionospheric effects in GPS time and frequency transfer, *GPS Solut.*, 14, 267–277, doi:10.1007/s10291-009-0152-1 , 2010.

Pramualsakdikul, S., R. Haas, G. Elgered and H.-G. Scherneck, Sensing of diurnal and semi-diurnal variability in the water vapour content in the tropics using GPS measurements, *Meteorol. Appl.*, 14, 403–412, doi:10.1002/met.39, 2007.

Ross, R.J., and W.P. Elliott, Tropospheric water vapor climatology and trends over north America: 1973–93, *J. Climate*, 9, doi:10.1175/1520-0442(1996)009<3561:TWVCAT>2.0.CO;2, 3,561–3,574, 1996

Ross, R.J., and W.P. Elliott, Radiosonde based northern hemisphere tropospheric water vapor trends, *J. Climate*, 14, 1,602–1,612, doi:10.1175/1520-0442(2001)014<1602:RBNHTW>2.0.CO;2, 2001.

Rummukainen, M., State-of-the-art with regional climate models, *Wiley Interdisciplinary 2 Reviews: Climate change*, 1(1), 82–96, 2010.

Rüeger, J.M., Report of the ad-hoc working party on refractive indices of light, infrared and radio waves in the atmosphere of the IAG Special Commission SC3-Fundamental Constants (SCFC), *Presented at the 22nd General Assembly of IUGS*, Birmingham, UK, July 18-30, 1999.

Saastamoinen, J., Atmospheric correction for the troposphere and stratosphere in radio ranging of satellites, in *The Use of Artificial Satellites for Geodesy, Geophys. Monogr. Ser.*, 15, edited by S.W. Henriksen et al., 247–251, AGU, Washington, D.C., 1972.

Saastamoinen, J., Contributions to the theory of atmospheric refraction, *Bull Géod*, 107, 13–34, doi: 10.1007/BF02521844, 1973.

Samuelsson, P., C. Jones, U. Willén, A. Ullerstig, S. Gollvik, U. Hansson, E. Kjellström, G. Nikulin, and K. Wyser, The Rossby centre regional climate model RCA3: model description and performance, *Tellus A.*, 63, 4–23, doi:10.1111/j.1600-0870.2010.00478.x, 2011.

Schmid, R., P. Steigenberger, G. Gendt, M. Ge, and M. Rothacher, Generation of a consistent absolute phase center correction model for GPS receiver and satellite antennas, *J. Geod.*, 81, 781–798, doi:10.1007/s00190-007-0148-y, 2007.

Sovers, O.J., J.L. Fanselow, and C.S. Jacobs, Astrometry and geodesy with radio interferometry: experiments, models, results, *Rev. of Modern Physics*, 70, 1393–1454, doi:10.1103/RevModPhys.70.1393, 1998.

Stoew, B., T. Nilsson, G. Elgered, and P.O.J. Jarlemark, Temporal correlations of atmospheric mapping function errors in GPS estimation, *J. Geod.*, 81(5), 311–323, doi:10.1007/s00190-006-0114-0, 2007.

Teunissen, P.J.G, and A. Kleusberg, GPS for Geodesy, *2th edition*, Springer, 1998.

Thomas, I.D., M.A. King, P.J. Clarke, and N.T. Penna, Precipitable water vapor estimates from homogeneously reprocessed GPS data: An intertechnique comparison in Antarctica, *J. Geophys. Res.*, 116, doi:10.1029/2010JD013889, 2011.

Thompson, A., J.M. Moran, and G.W.S. Jr, Interferometry and synthesis in radio astronomy, *2nd ed.*, John Wiley & sons, New York, 2001.

Titchner, H.A., P.W. Thorne, M.P. McCarthy, S.F.B. Tett, L. Haimberger, and D.E. Parker, Critically reassessing tropospheric temperature trends from radiosondes using realistic validation experiments, *J. Clim.*, 22, 465–485, doi:10.1175/2008JCLI2419.1, 2009.

Trenberth, K.E., A. Dai, R.M. Rasmussen, and D.B. Parsons, The changing character of precipitation, *Bull Amer Meteor Soc.*, 84(9), 1,205–1,217, doi:10.1175/BAMS-84-9-1205, 2003.

Trenberth, K.E., L.Smith, T. Qian, A. Dai, and J. Fasullo, Estimates of the global water budget and its annual cycle using observational and model data. *J. Hydrometeor.*, 8, 758–769, doi:10.1175/JHM600.1, 2007.

Treuhaft, R.N., and G.E. Lanyi, The effect of the dynamic wet troposphere on radio interferometric measurements, *Radio Sci.*, 22(2), 251–265, doi:10.1029/RS022i002p00251, 1987.

Wang, J., L. Zhang, and A. Dai, Global estimates of water-vapor-weighted mean temperature of the atmosphere for GPS applications, *J. Geophys. Res.*, 110, doi: 10.1029/2005JD006215, 2005.

Wang, J., L. Zhang, A. Dai, T.V. Hove, and J.V. Baelen, A near-global, 2-hourly data set of atmospheric precipitable water from ground-based GPS measurement, *J. Geophys. Res.*, 112, doi: 10.1029/2006JD007529, 2007.

Wang, J., and L. Zhang, Systematic errors in global radiosonde precipitable water data from comparisons with ground-based GPS measurements, *J. Clim.*, 21(10), 2,218–2,238, doi:10.1175/2007JCLI1944.1, 2008.

Wang, J., and L. Zhang, Climate applications of a global, 2-hourly atmospheric precipitable water dataset from IGS round-based GPS measurements, *J. Geod.*, 83, 209–217, doi:10.1007/s00190-008-0238-5, 2009.

Weatherhead, E.C., G.G. Reinsel, G.C. Tiao, X-L. Meng, D. Choi, W-K. Cheang, T. Keller, J. DeLuisi, D.J. Wuebbles, J.B. Kerr, A.J. Miller, S.J. Oltmans, and J.E. Frederick, Factors affecting the detection of trends: Statistical considerations and applications to environmental data, *J. Geophys. Res.*, 103(D14), 17,149–17,161, doi:10.1029/98JD00995, 1998.

Wolf, H., Determination of water density: limitations at the uncertainty level of 1×10^6, *Accred Qual Assur*, 13, 587–591, doi:10.1007/s00769-008-0442-2, 2008.

Webb, F.H., and J.F. Zumberge, An introduction to the GIPSY/OASIS II, *JPL Publ.*, D11088, 1993.

Wyser, K., C.G. Jones, P. Du, E. Girard, U. Willén, J. Cassano, J.H. Christensen, J.A. Curry, K. Dethloff, J.-E. Haugen, D. Jacob, M. Køltzow, R. Laprise, A. Lynch, S. Pfeifer, A. Rinke, M. Serreze, M.J. Shaw, M. Tjernström, and M. Zagar, An evaluation of Arctic cloud and radiation processes during the SHEBA year: simulation results from eight Arctic regional climate models, *Clim. Dyn.*, 30, 2–3, 203–223, doi:10.1007/s00382-007-0286-1, 2008.

Zumberge, J., M. Heflin, D. Jefferson, M. Watkins, and F. Webb, Precise point positioning for the efficient and robust analysis of GPS data from large networks, *J. Geophys. Res.*, 102, 5,005–5,017, doi:10.1029/96JB03860, 1997.